UNIVERSITY OF OKLAHOMA

GRADUATE COLLEGE

RELFECTION SEISMIC INVESTIGATION OF AN ALPINE VALLEY IN UNAWEEP CANYON, WESTERN COLORADO: EVIDENCE OF PALEOZOIC GLACIATION OF THE UNCOMPAHGRE PLATEAU

A THESIS

SUBMITTED TO THE GRADUATE FACULTY

in partial fulfillment of the requirements for the

Degree of

MASTER OF SCIENCE

By

ANNA PATTERSON
Norman, Oklahoma
2019

REFLECTION SEISMIC INVESTIGATION OF AN ALPINE VALLEY IN UNAWEEP CANYON, WESTERN COLORADO: EVIDENCE OF PALEOZOIC GLACIATION OF THE UNCOMPAHGRE PLATEAU

A THESIS APPROVED FOR THE
CONOCOPHILLIPS SCHOOL OF GEOLOGY AND GEOPHYSICS

BY

Dr. Michael Behm, Chair

Dr. Gerilyn Soreghan

Dr. Heather Bedle

© Copyright by ANNA PATTERSON 2019
All Rights Reserved.

Acknowledgements

I want to thank Iris Pascal Instrument Center and the Seismic Source Facility for use of equipment and personnel during the acquisition of the data. I especially want to thank Dr. Galen Kaip and Dr. Steven Harder for their expertise and assistance during the acquisition. And thanks for the use of funds from NSF-EAR-1338331 for the partial funding of this project. Also thanks to Dr. Michael Behm, Dr. Gerilyn (Lynn) Soreghan, Dr. Jefferson Chang, Dr. Feng Cheng, and Pranshu Ratre for their hard work during the acquisition, and the town and community of Gateway, Colorado for their support throughout the acquisition.

I want to thank my committee, Dr. Michael Behm, Dr. Gerilyn (Lynn) Soreghan, and Dr. Heather Bedle, for all their help and support along the way during this process. I especially want to thank Dr. Michael Behm for taking a chance on me even though I had never taken a geophysics class before and for being patient to answer all my questions.

I especially want to thank Dr. Werner Chwatal and his patience in teaching me the steps of processing and for checking over my work. Thank you for taking the time out of your day to answer questions and to teach me the different imaging techniques used in alpine valleys in Austria.

Lastly, I want to thank my parents and boyfriend for always believing and supporting me in all that I have done.

Table of Contents

List of Equations

List of Figures

Abstract

Unaweep Canyon in Western Colorado is a unique landscape which has a puzzling history. The canyon has a wide U-shaped profile in the west that contrasts with the narrow V-shaped river carved canyons nearby. Many suggest that the canyon was carved by the ancestral Gunnison River and then later abandoned, but this hypothesis does not support all the canyon's geomorphologic features. Others have suggested that due to the canyon's unique U-shaped profile and other glacial geomorphologic features, that the canyon was carved initially by a late Paleozoic glaciation and later exhumed by the ancestral Gunnison River. This hypothesis is highly contested since this region of western Colorado was equatorial during the late Paleozoic, and climate models do not support equatorial glaciation in the late Paleozoic. Previous work including shallow seismic, drilling and a gravity survey determined that there is a thick sediment fill hiding the Precambrian basement geometry. Understanding the geometry is critical in determining how the canyon formed. Further seismic work was needed to delineate the basement geometry.

Active reflection seismic was used to obtain a high resolution and clear image of the Precambrian basement to aid in the investigation of the genesis of the canyon. A 2.45 km seismic line was acquired across the broadest part of Unaweep Canyon. First arrival tomography was used to create a smooth velocity model of the shallow subsurface. The lack of fast velocities imaged in the southern segment of the tomographic model suggest over-deepening of the Precambrian basement. The results from the reflection seismic confirm an over deepening of the Precambrian basement with a precise U-shaped geometry, and a basement depth of ~450 m in the over-deepened portion. Due to lack of significant faulting seen in the survey and lack of glaciation during the Quaternary, the structure is interpreted to be an alpine glacial valley

supporting the hypothesis of glaciation during an earlier interval of Earth history—most likely the late Paleozoic. This evidence is in contrast with current climate models of the late Paleozoic which fail to depict glaciation in equatorial uplands.

Chapter 1: Introduction

1.1 Geology

The first person known to document the geology of Unaweep Canyon was Peale (1877) as a part of the Hayden Survey, the first geologic survey conducted in Wyoming and Colorado in 1869. Unaweep Canyon is ~70 km long and bisects the western part of the Uncompahgre Plateau (Figure 1a, Cole and Young, 1983). The Uncompahgre Plateau is a northwest-trending uplift in Western Colorado, bounded in the southwest and northeast by faulted monoclines (Cater, 1966). The Uncompahgre Plateau is within the larger Colorado Plateau which saw recent uplift between the Late Cretaceous to early Tertiary with the amount of uplift still debated (McQuarrie and Chase, 2000). The canyon is carved into Mesozoic and Precambrian rock and is ~1 km deep from rim to the canyon floor and ~6 km wide in the western stretch (Figure 1a; Cole and Young, 1983). In the far northeastern portion, the canyon has a narrow V-shape characteristic and is cut mostly into Mesozoic sediments. The northeast portion is ~150 m deep from rim to the canyon floor and ~1.3 km wide from rim to rim (Cole and Young, 1983).

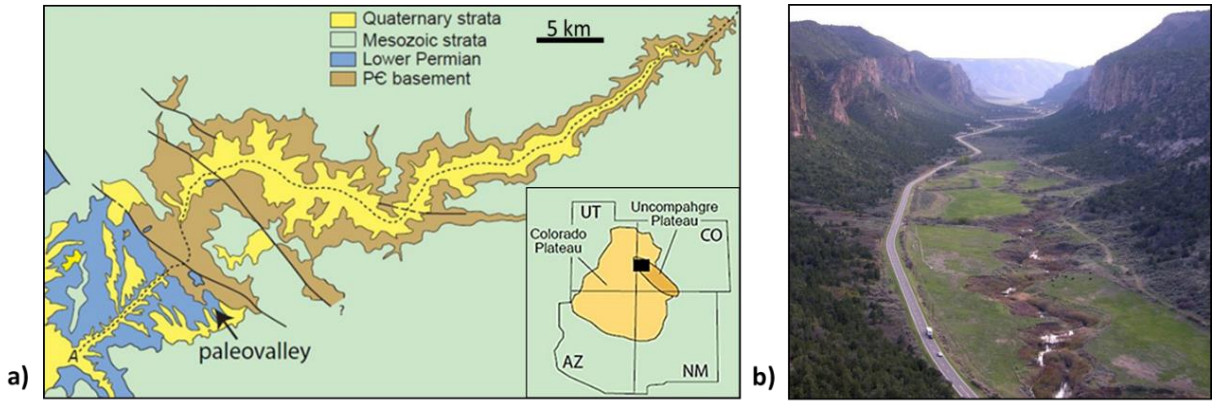

Figure 1: Overlook of Western Portion of Unaweep Canyon and Geologic Map
1a modified from Soreghan et al. (2015) displays a simplified geologic map of Unaweep Canyon. 1b shows the western portion of the canyon. The steep nearly vertical walls emphasize the U-shaped profile (Photo by G. Soreghan).

Unaweep Canyon has a distinct U-shape in the western portion that some have noted to be reminiscent of a glacial valley (Figure 1b; Lohman, 1981; Cole and Young, 1983). Cole and Young (1983) suggested a possible Quaternary glacial origin by highlighting geomorphologic features throughout the canyon such as possible cirques, truncated spurs, and hanging valleys, in addition to the apparent U-shape. Quaternary glaciation seems unlikely since Unaweep Canyon

has a relatively low elevation (~2148 m at Unaweep Divide) compared to the lowest extent of ice known from Pleistocene glaciations in the region (~2750 m; Yeend, 1969). Additionally, there are no Quaternary glacial deposits within or surrounding the canyon (Lohman, 1981; Scott et al., 2001; Soreghan et al., 2007).

The canyon hosts two small creeks, East and West creek that flow in opposite directions from a drainage divide in the middle of the canyon. The divide creates a canyon with two mouths-- the only known canyon with this feature in the world. Either end of the canyon sits at ~1500 m elevation while the drainage divide is ~2100 m (Cole and Young, 1983). All agree that the current creeks are not powerful enough to have carved the canyon meaning that the canyon has been abandoned by the process that created it (Cater, 1966) and leading to multiple different hypotheses of how the canyon formed and what ancestral river originally traversed it.

1.2 Formation Hypotheses

Initial formation hypotheses for Unaweep Canyon concentrated on determining the river that once flowed through the canyon. Early hypotheses were the ancestral Gunnison River (Peale, 1877) the ancestral Colorado River (Gannett, 1882), or a combination of both (Gannet, 1882). Later work has shown that the ancestral Gunnison River did flow through the canyon (Cater, 1966; Soreghan et al., 2007; Aslan et al., 2014; Price et al., 2012; Soreghan et al., 2015), and later abandoned it, but the debate on the canyon's origin remains, owing to the geomorphologic features of the sidewalls. Soreghan et al. (2007, 2008, 2014, 2015) argued that Unaweep Canyon was carved by late Paleozoic (Pennsylvanian-Permian) glaciation, buried, and then exhumed by the ancestral Gunnison River before river abandonment in the early Pleistocene (Balco et al., 2013). A glacial origin and late Paleozoic age are criticized by many being highly improbable (Aslan et al., 2008, 2014; Hood et al., 2009). During the late Paleozoic, this part of North America was within ~8^{o} of the equator (Soreghan et al., 2007), and coastal plain facies are

within 65 km from the canyon (Condon, 1997). Modern equatorial glaciers thrived around 3400-4400 m elevation during Quaternary glaciations (Porter, 2000), but these elevations exceed those presumed for the Paleozoic Uncompahgre uplift.

1.3 Previous Work

Previous geophysical work in Unaweep Canyon has shed some light on the subsurface here (Figure 2). Refraction and 1D resistivity surveys indicated that the canyon had a thick sediment fill (Oesleby, 1978) which was further established by two gravity lines suggesting sediment fill ~390 m thick locally (Davogustto, 2006). A well drilled in 2004 proved that the canyon has thick sediment fill at least 320 meters deep, obscuring the Precambrian basement geometry (Soreghan et al., 2007). The core of the well revealed three distinct layers with a 7-meter transition from the upper to a middle unit consisting of mostly paleosols (Soreghan et al., 2007). The top layer comprises Pleistocene fanglomerate that also covers the canyon's modern floor (Soreghan et al., 2007). The middle layer records Pleistocene lacustrine deposition—a result of damming of the ancestral Gunnison River (Soreghan et al., 2007, 2015; Marra, 2008; Balco et al., 2013). The core terminated in a diamictite containing large Precambrian basement clasts in a finer matrix (Soreghan et al., 2007). This lowest layer is interpreted to be late Paleozoic in age since it contains Paleozoic pollen and no Mesozoic clasts and exhibits low magnetic inclinations (Soreghan et al., 2007). A late Paleozoic age is debated since the layer also contained Quaternary pollen (Soreghan et al., 2007) which some consider indicating the actual age of the layer and the Paleozoic sediments are reworked (Hood et al., 2009). The thickness of the sediment layer leads to the idea that the Precambrian basement might be over-deepened which would confirm a glacial origin (Soreghan et al., 2015). Over-deepening means that the Precambrian basement is carved below the local fluvial grade which is a common characteristic

of glacial valleys (Linton, 1963). If there are no structural reasons from the over-deepening, this will strengthen the hypothesis that the canyon had a glacial origin since rivers are incapable of flowing upslope.

Two reflection lines were acquired in 2004, in the inline and crossline direction of the canyon to determine the Precambrian basement structure (Figure 3, Rojas, 2007). The inline was 560 m long while the crossline was 118 m. Both surveys had a weak signal to noise ratio of the data, limiting the visibility of the Precambrian basement structure (Figure 3). Limited visibility is attributed to using a lower energy source (Betsy Gun), and the survey length limiting long offsets (Rojas, 2007). There were irregularities in the basement reflector leading to the conclusion that either the basement is faulted in the area following regional fault trends or an indication of glacial erosional features (Rojas, 2007). Further ray tracing models showed that the basement reflector comes from a U-shaped structure with flat sediment fill within the canyon (Figure 3, Rojas, 2007). A gravity survey completed in 2014, suggested that the Precambrian basement was over-deepened but could not confirm a U or V-shaped geometry (Figure 4; Haffener, 2015).

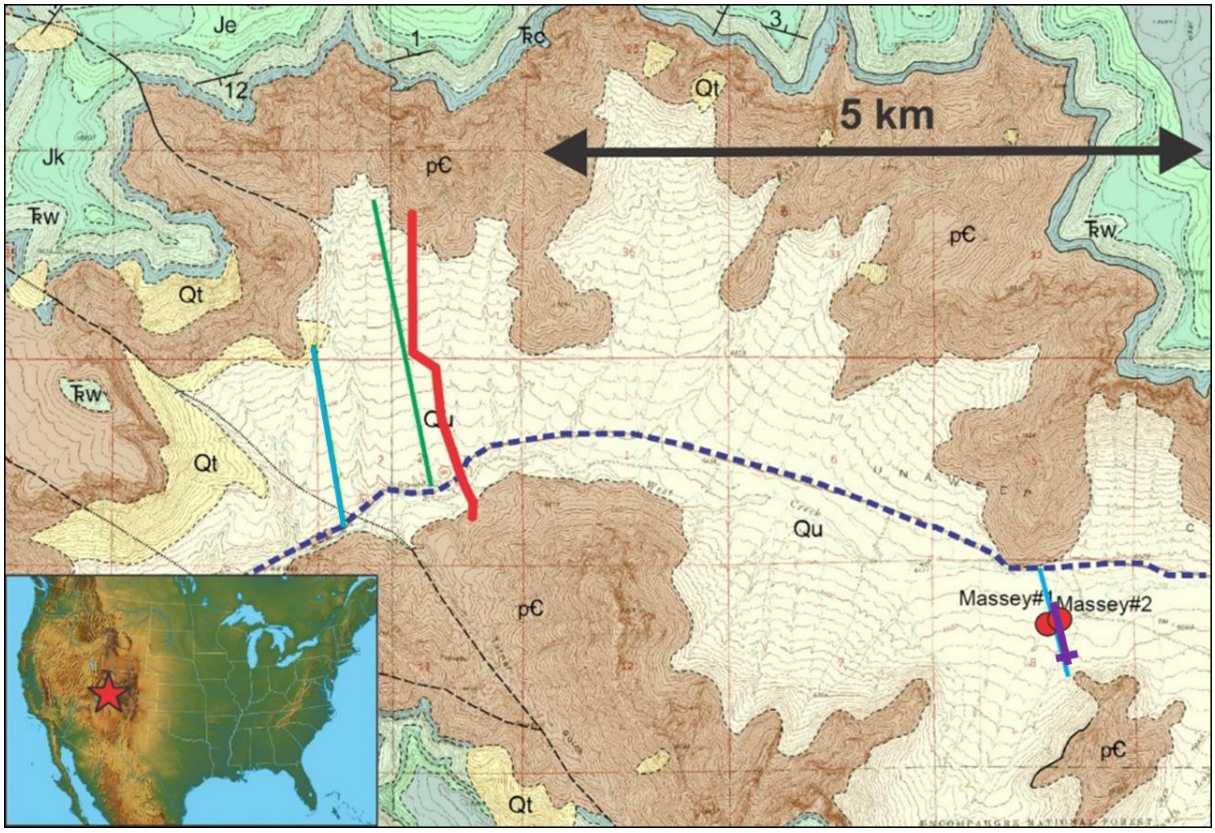

Figure 2: Geologic Map displaying the location of previous studies.
Geologic map created by Eccles, T.M, Soreghan, G.S., Kaplan, S.A., Patrick, K.D., and Sweet, D.E. The location of previous geologic and geophysical surveys are displayed. The blue lines are the gravity lines from Davogustto (2006). Purple represents the reflection lines from Rojas (2007). Green is a gravity line from Haffener (2015). Red is the reflection acquisition from this study. The red dots represent the core location from the Massey wells.

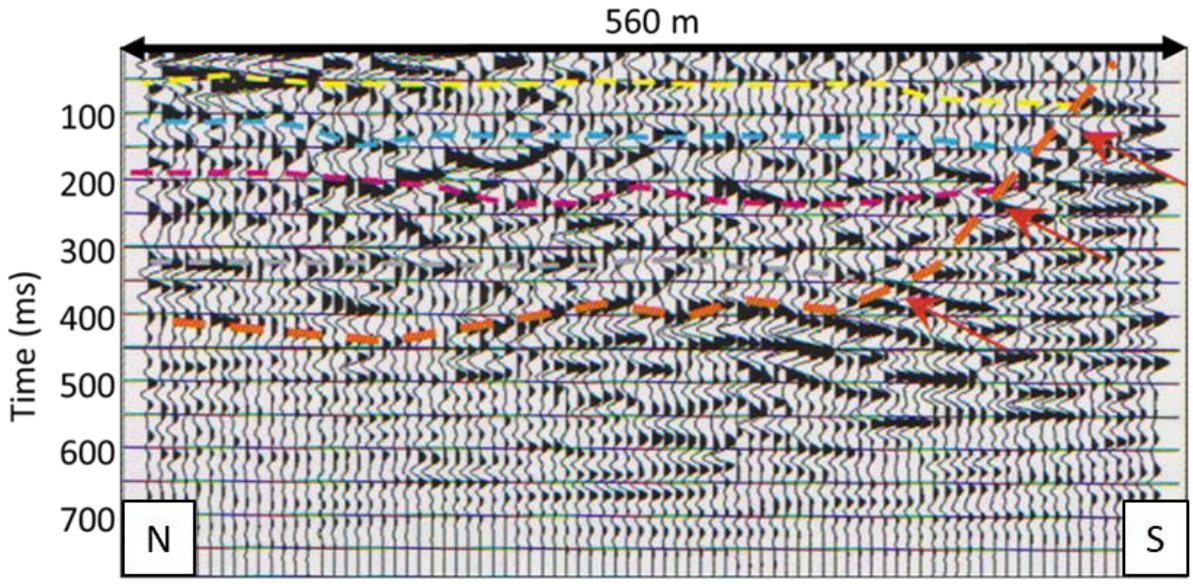

Figure 3: Rojas (2007) results in the inline reflection survey. The data has a poor signal to noise quality affecting the interpretation. The interpretation of the Precambrian basement (red) and sediment layers (yellow, blue, pink) are determined through ray tracing modeling. The red arrows indicate the possible steep dip of the basement structure.

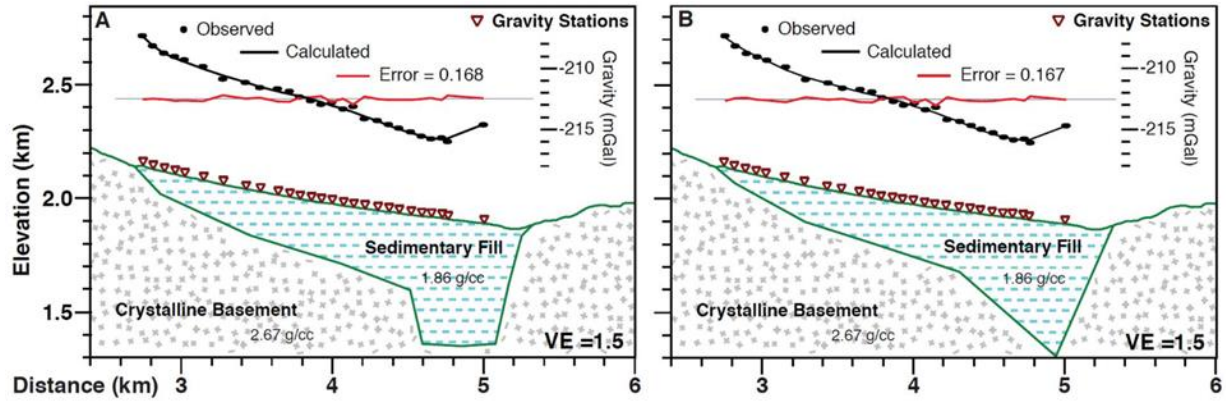

Figure 4: 2014 Gravity Survey
Gravity results from Haffener (2015). Both an over-deepened U-shaped and over-deepened V-shaped geometry was modeled. The data only fit the models with over-deepening.

1.4 Aim of Thesis

From the previous studies, the hypotheses that the canyon had a thick sediment fill (Oesleby, 1978; Davogustto, 2006) were confirmed with the drilling of two wells (Soreghan et al., 2007) leading to the idea of over-deepening of the Precambrian basement caused by glacial processes (Soreghan et al., 2008). If the Precambrian basement elevation within the canyon is below the elevation of the basement outcrops at each mouth of the canyon, that would support over-deepening. However, no survey has been able to display a clear image of the Precambrian basement to prove over-deepening and to delineate whether the basement geometry is U or V-shaped.

Work conducted in this thesis aims to understand the basement geometry better and subsequently how the canyon formed through the reflection seismic method. The reflection seismic method has been successfully used in other alpine valleys throughout the world to determine the origin (e.g., de Franco et al., 2009; Brueckl et al., 2010; Bleibinhaus and Hilberg, 2012; Pomper et al., 2017). The goal of this thesis is to confirm or reject the suggested over-deepening of the Precambrian basement and to determine the basement structure. Answering these questions will determine if the canyon has a glacial or fluvial origin. The total depth of sediments will also be determined to understand the thickness of the sedimentary fill.

Chapter 2: Data Acquisition

A 2D reflection seismic acquisition was planned in west Unaweep Canyon to delineate the Precambrian basement geometry (Figure 2). The line is 2.45 km long positioned along the widest part of the canyon near the 2014 gravity line and 5 km west of previous cored wells (Figure 2). The survey was planned along a 4x4 road to allow usage of a truck-mounted source. An active gravel mine is to the southwest of the line and acquisition was limited to the weekend to avoid noise from this area. The acquisition including set up, shooting, pick up, and downloading of the data was performed on September 29th - October 1st of 2017, with nine field workers. Each shot and receiver location were surveyed with differential GPS, resulting in accuracies of a few centimeters

2.1 Receivers

The type of receiver used for an experiment depends on the environment and goals of the project. A geophone is the most common receiver used for land acquisitions and consists of a coil of wire suspended by a spring around a magnet separating the north and south end. As the ground moves up and down the magnet moves with it moving the magnetic field. The relative movement of the magnetic field to the stationary coil induces a voltage that is transmitted in a data logger as the signal. Receivers have their natural frequency (e.g., 4.5 Hz, 10 Hz, 30 Hz), depending on the design of the geophone.

Choosing a natural frequency allows the user to limit the amount of noise in a particular frequency band. Receivers with low natural frequency are better suited for recording surface waves, whereas receivers with high natural frequencies record reflections better. Recordings below the natural frequency are damped (lower amplitude), and do not override the wanted signal (Maxwell and Lansley, 2011). Geophones for oil and gas explorations usually have a

natural frequency of 10 Hz to limit low frequencies like ground roll and to better record high frequencies, increasing resolution (Maxwell and Lansley, 2011). Since the goal of this project was to image the large-scale structure of the basement and not to create a high-resolution image of the shallow subsurface, low natural frequency geophones were used.

Two types of receivers were used in the acquisition: Fairfield Zland 3C nodes and 1C geophones (Figure 5) programmed with a 1 ms sampling rate. There were 120 Fairfield ZLand 3C nodes with a natural frequency of 5 Hz. 3C stands for three components, which means they can record both vertical and horizontal components of the wave field. Only the vertical component processing was within the scope of this study. These nodes can record for up to a month continuously, so they were set out and recorded during the entire deployment period. The nodes were deployed on the northern portion of the line.

Additionally, there were 385 1C geophones (natural frequency of 4.5 Hz) connected to Texan data loggers. These are sensitive to vertical ground movements only. The Texans run off two D-cell batteries and to ensure the batteries lasted the entire acquisition they were pre-programmed to turn on only during the day. The Texans were used on the remaining part of the line.

There were 505 recording stations total at 5 m spacing (Figure 8). Station locations were labeled *0 - 2495* starting with *0* in the northern portion of the line. Stations across the highway and the creek were not set up with geophones (2090 - 2095, 2105 - 2110, 2200, 2230 - 2235). Fairland nodes were located at stations 0 - 620 while Texans were located at stations 625 - 2495. Total line length was 2.45 km.

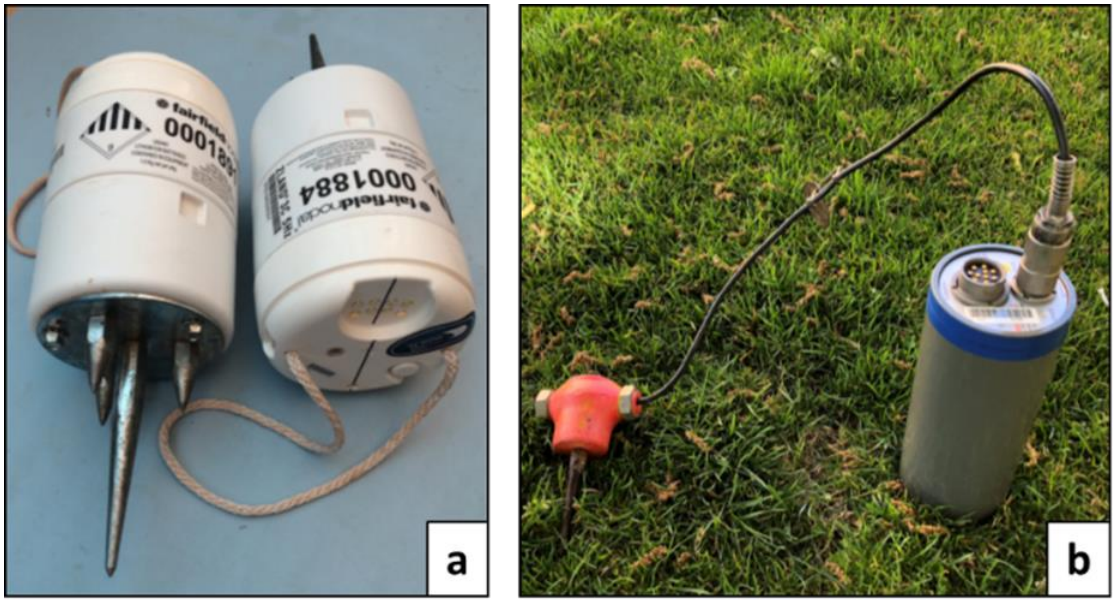

Figure 5: Receivers
Fairfield 3C Nodal receivers (a), and 1C geophones connected to a Texan data logger (b) used in the acquisition.

2.2 Source

The primary source used for the survey was a nitrogen pressure A200 P&S impact source (Figure 6; Lawton et al., 2013). The source was mounted on the back of a truck with full water tanks to help prevent the truck from bouncing during each shot, limiting noise. The source consisted of a footplate coupled to the ground. A nitrogen-pressured pistol fired into the hammer to create the seismic source signal. Several piston strikes were used to ensure the hammer was well coupled to the ground before the shots used for the data were recorded. This source has repeatable energy outputs and quick succession between shots, making it an ideal source for environmental settings and target depth similar to those in this study. The truck was kept running at all times due to time constraints; this created some noise in the data.

A sledgehammer with a metal strike plate was used for supplemental shots in the northern segment of the survey beyond road access (Figure 6). Sledgehammers are not a consistent source

since they rely on human execution and are not as powerful as the truck-mounted source. The waves attenuate faster, and depth penetration and resolution are decreased compared to the truck-mounted source.

Figure 6: Sources
Images of the sledgehammer and strike place (a) that was implemented in the northern portion of the survey. 6b, c, and d display the P&S truck-mounted impact source that was used for the survey. The foot plate of the impact source is coupled to the ground, and then a nitrogen-pressured piston is shot into the footplate which transmits seismic waves into the ground.

2.3 Shots

There were 264 individual shot locations as seen in Figure 8. Shot times were recorded via a trigger and GPS stamp. At each truck mounted source location at least five individual blasts were done while four were done for sledgehammer locations. Individual blasts were stacked to increase the signal to noise ratio for individual shot gathers. Shots were performed in-between stations (2.5 meters away from geophones and slightly to the east of the line) and labeled with the lower station number +20000 (Figure 7). Shots 20005 - 20395 were done by sledgehammer while Shots 20405 - 22425 were done by the truck-mounted impact source. In the northern segment of the profile before station 1785 (Shot 21785), shots were located at 10 m spacing. After Shot 21785, shots were spaced at 5 m to acquire higher fold in the area where the sediment fill is expected to be thickest based on previous surveys. On the first day of shooting (September 30th), Shots 20405 to 22425 were acquired. Shot locations positioned on the road, steep slopes or within the creek where the truck could not drive were skipped (shot locations 22015 - 22040, 22065 - 22095, 22240 - 22380, 22430 - 22495) Shot locations 21865 - 22425 (new shot numbers 31865-32425) were repeated on October 1st. The first shots were done with the source at a higher power level causing the truck to bounce and creating more noise. During active shooting, both sledgehammer and truck-mounted shots were performed simultaneously due to time constraints. Care was taken to make sure the two sources were far enough away from each other, but some overlap occurred.

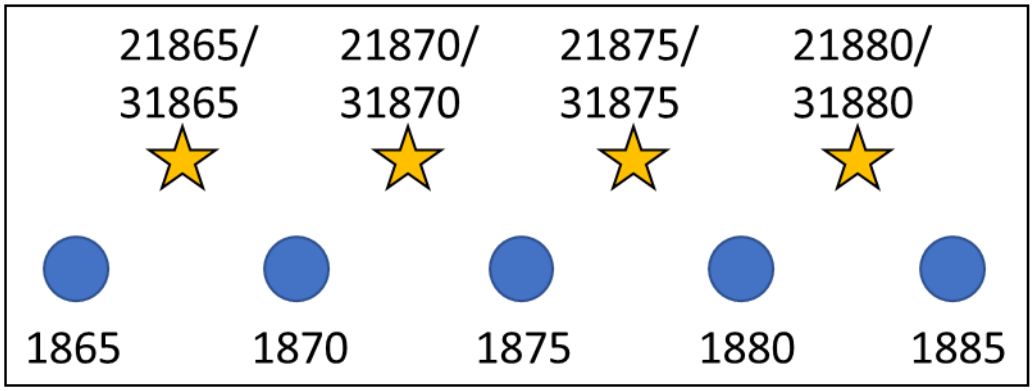

Figure 7: Shot Numbering
Receivers (blue dot) are labeled with the distance along the line. Shot locations (stars) are halfway between two receiver locations and off to the side. The shot locations are labeled with the lower station number +20000.

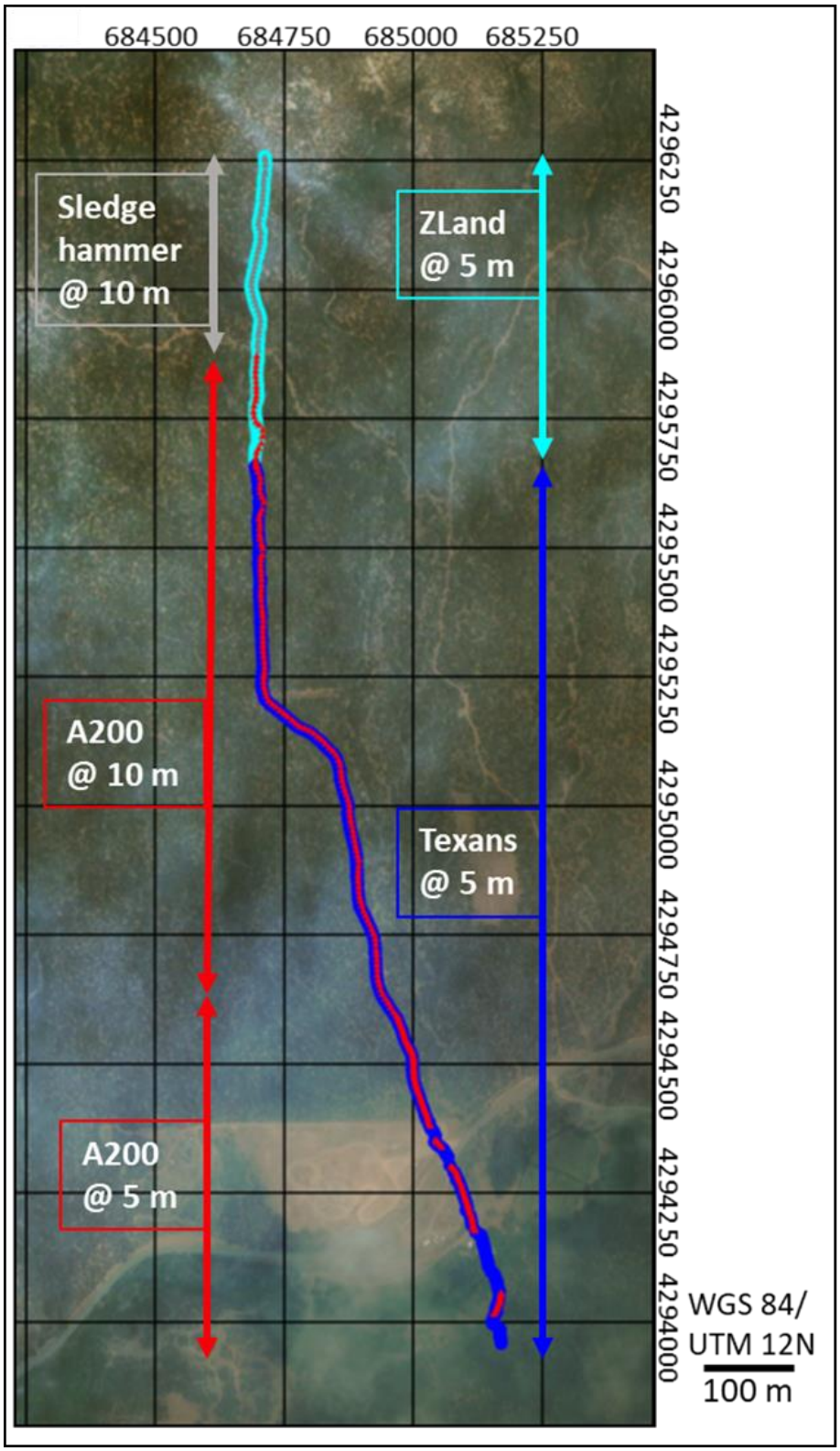

Figure 8: Acquisition Layout
Acquisition map displaying the geometry of the line and locations of all shots and receivers. The background is a satellite image of Unaweep Canyon.

2.4 Raw Data

Noise

Our survey crossed State Highway 141 in the south, which had little traffic during shooting but still contributed noise. A creek ran through the survey in the south adding noise in that area. The noise created by the truck carrying the source can also be seen within the data. Other noise, including footsteps, are present throughout the data since there was a tight schedule and some activities were done simultaneously (Figure 9a). Sledgehammer shots and truck-mounted source shots were done concurrently, and there is some overlap seen in the shot gathers (Figure 9b). Overall, the data has a high signal to noise ratio. There is also an improvement of the signal-to-noise from the sledgehammer source to truck-mounted source (Figure 10).

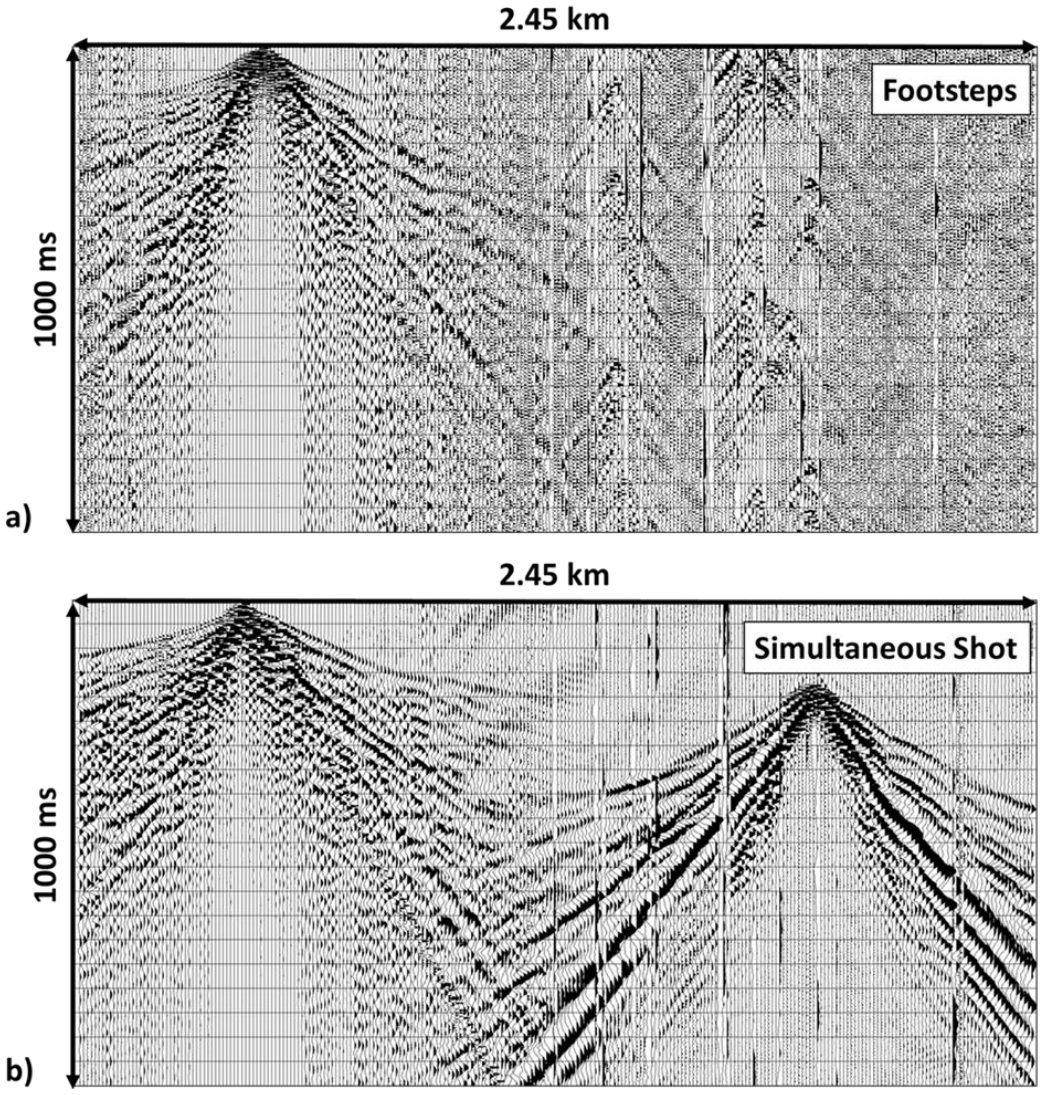

Figure 9: Shot Gathers displaying noise
Shot gather 20245 (a), and 20415 (b) show examples of footsteps and simultaneous shooting within the survey. Location of shot gathers within the survey shown in Figure 13. Ormsby bandpass filter of 15-30-90-120 was applied.

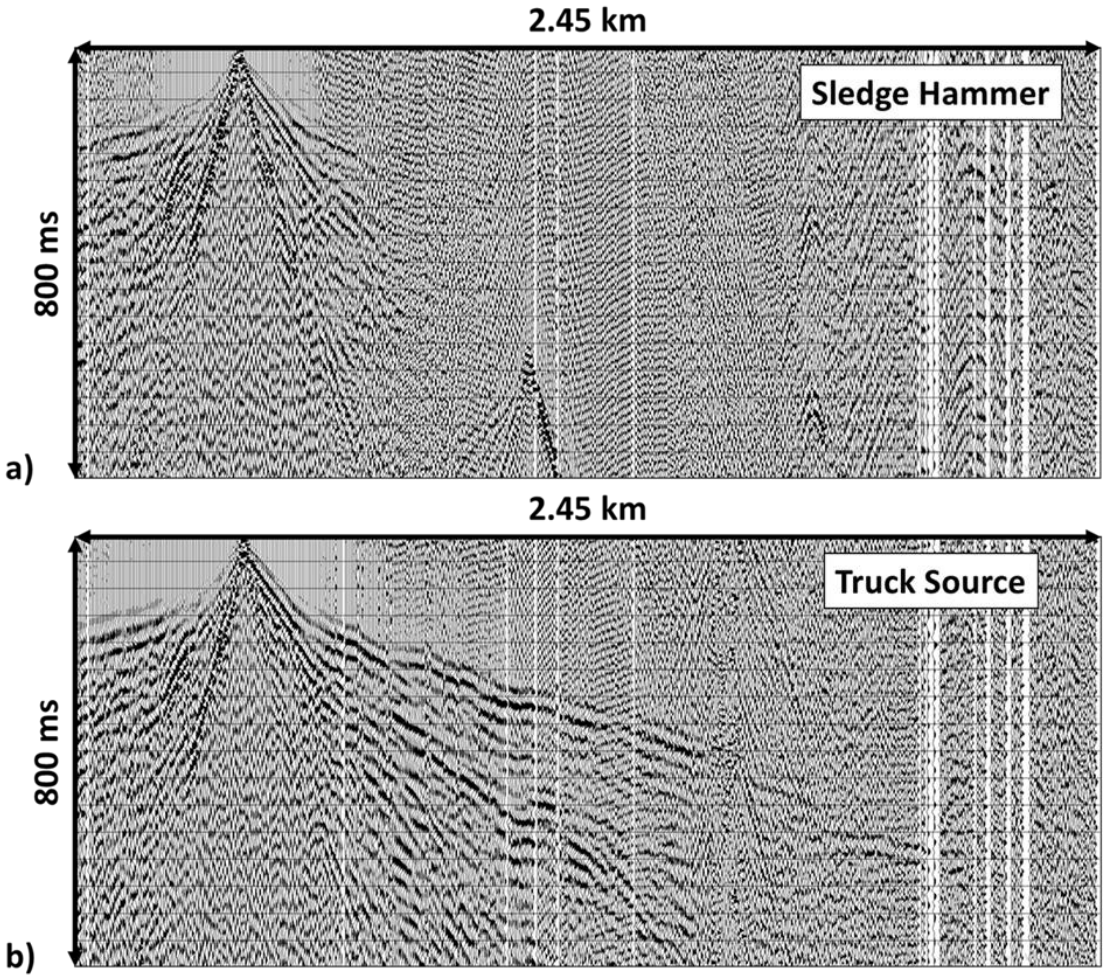

Figure 10: Truck vs. Hammer Shot Gather
Shot gather 20395 (a), and 20405 (b) displays the signal to noise difference between sledgehammer source and truck-mounted impact source. The first arrivals from the truck source have larger offsets than the sledgehammer. Location of shot gathers within the survey shown in Figure 13. Ormsby bandpass filter of 15-30-90-120 was applied.

First Arrivals

Shot gathers represent the recordings (traces) at all receivers from one single shot. The first arrivals have a maximum offset of 1.5-2 km when the truck mounted source was used (Figure 11a). There is a clear break in slope of the first arrivals within the shot gathers representing the difference of velocities from the sediments to the Precambrian basement (Figure 11b). The apparent velocities of sediment fill averages to ~800-1500 m/s whereas ranges for

Precambrian basement are ~3400-5000 m/s (Figure 11a). Apparent velocity is the seismic wave speed in the direction of offset and related to the true velocity of the layer. Apparent velocity is usually different than true velocity if there is a dip due to changes in the travel path. Up-dip shooting increases the apparent velocity while down-dip shooting decreases the apparent velocity.

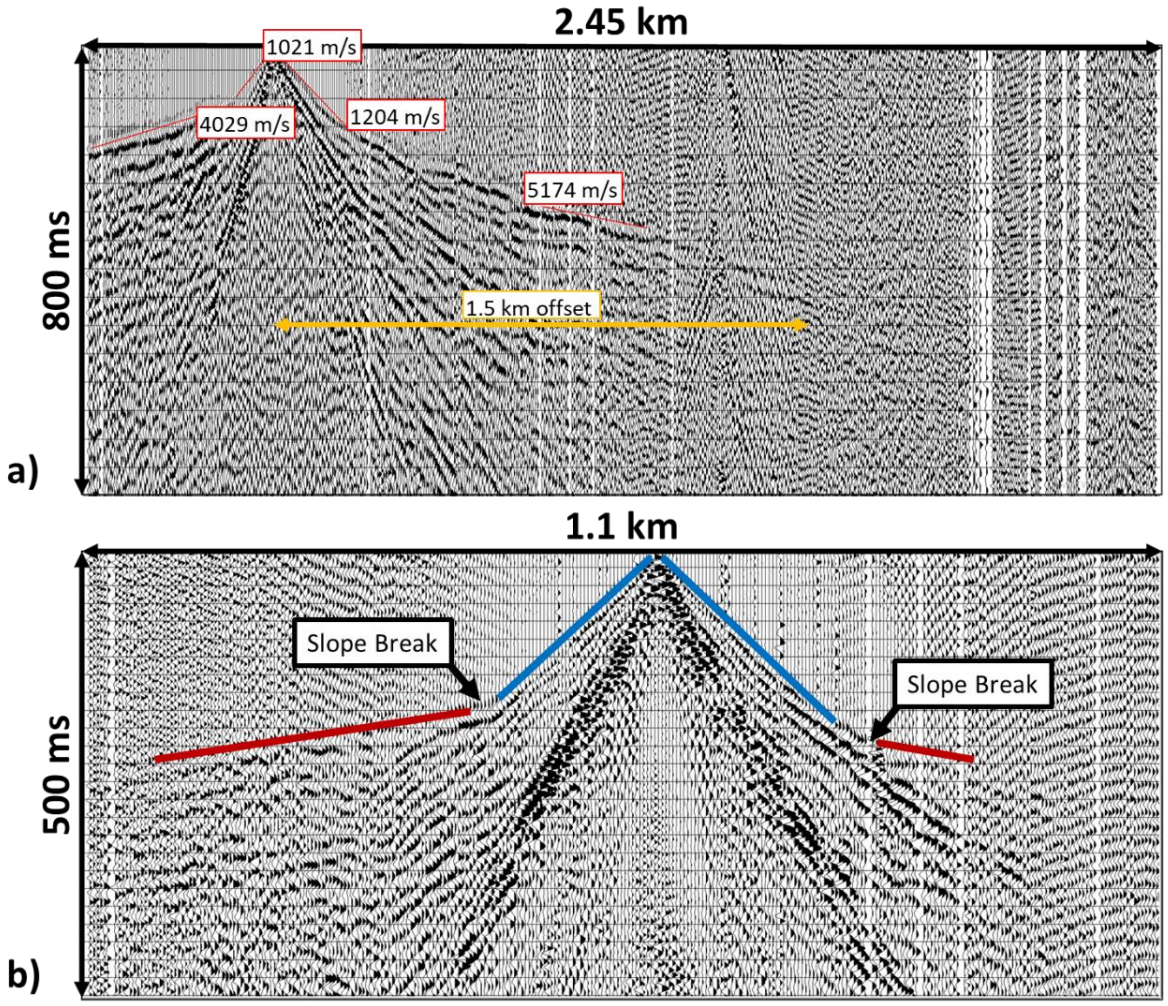

Figure 11: Shot Gather displaying first arrivals
Shot gather 20425 (a) displays examples of the first arrival apparent velocities. Shot gather 20765 (b) shows examples of the first arrival picks and the slope break between the sediment arrivals (blue) and Precambrian basement arrivals (red). Location of shot gathers within the survey shown in Figure 13. Ormsby bandpass filter of 15-30-90-120 was applied.

First Arrival and Reflection Geometry

Noticeable in the shot gathers is the difference in arrival times for the basement on either side of the shot gathers. The time differences give an asymmetry to them that is visible in all the gathers but is more pronounced on the southern portion of the survey (Figure 12). If the structure in the Precambrian basement were the same across the line, the basement arrivals would appear at the same time on both sides of the shot gathers, creating a symmetrical appearance of the arrival move-outs. The differences in arrivals suggest that the Precambrian basement has a complex structure. Deeper reflections also have an asymmetry inferred to reflect steep dips in the Precambrian basement structure (Figure 12).

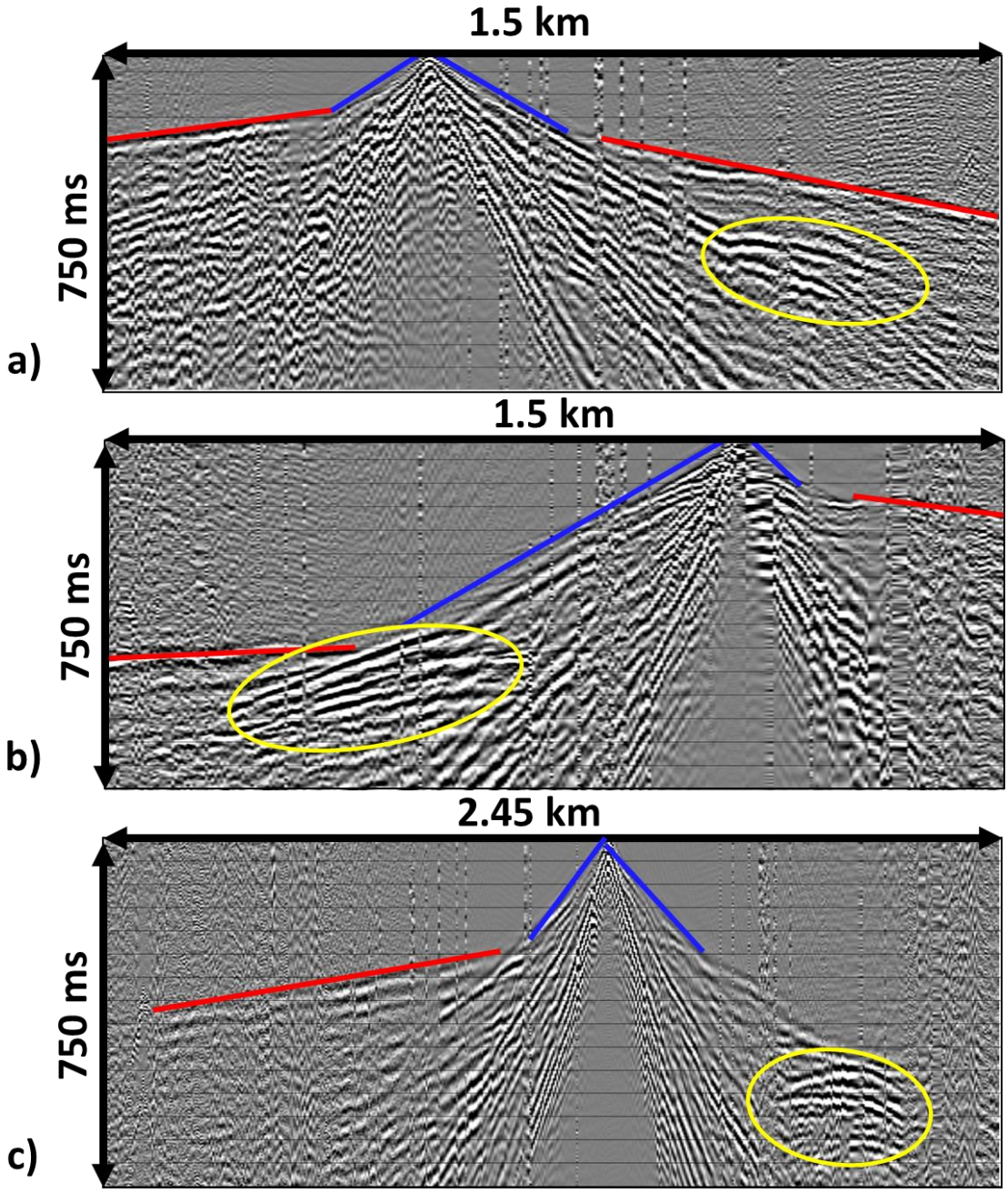

Figure 12: Shot Gather displaying Deep Reflections
Shot gather 20565 (a), 32055 (b), and 21405 (c) display the presence of deeper reflections. Location of shot gathers within the survey shown in Figure 13. Ormsby bandpass filter of 15-30-90-120 was applied.

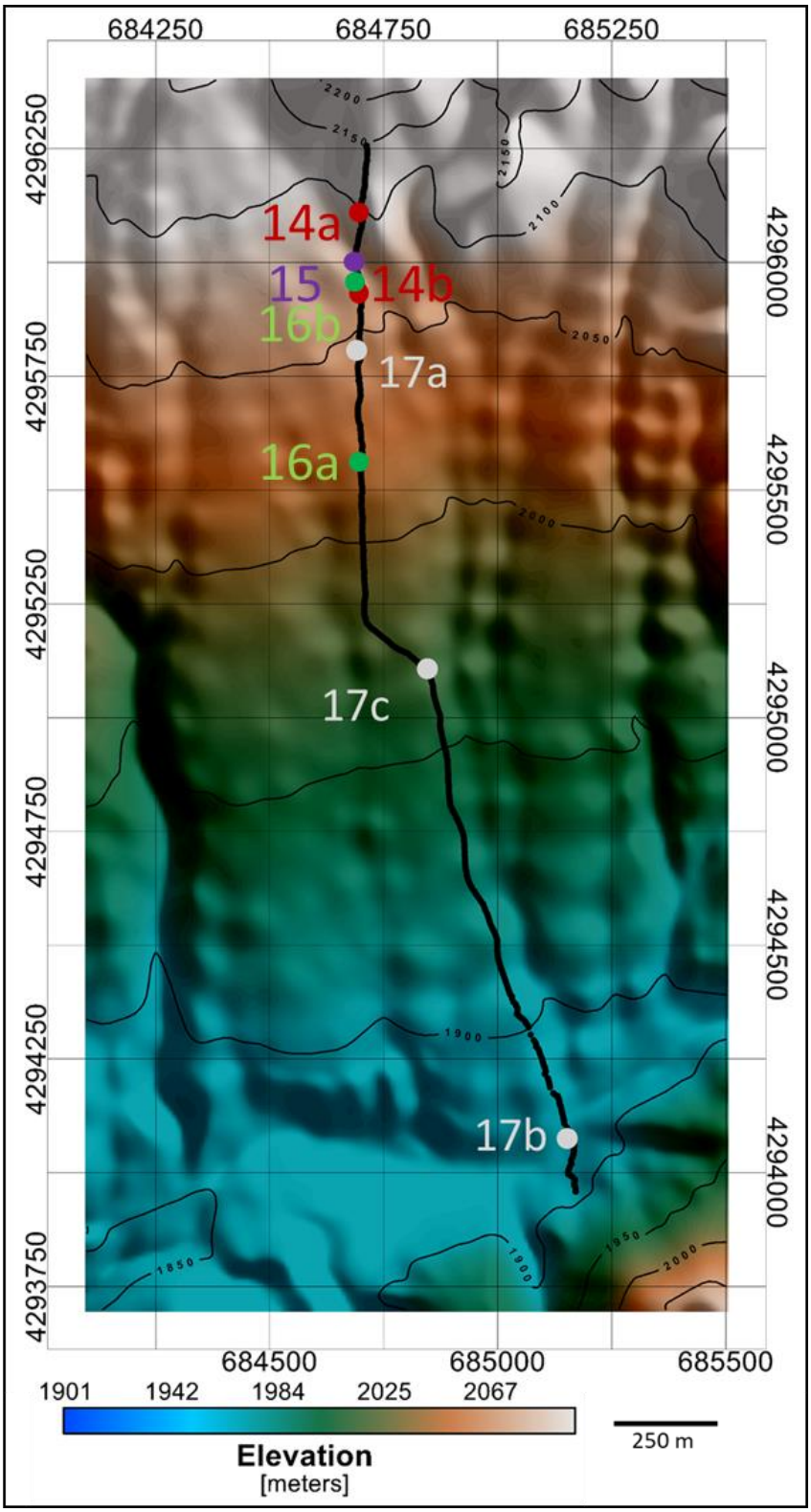

Figure 13: Digital Elevation Model (DEM)
The acquisition background with the digital elevation model of the canyon. The location of the shot gathers presented in Figures 14, 15, 16, and 17 are highlighted.

Chapter 3: First Arrival Tomography

First arrival tomography uses the arrival times of the refractions to determine a smooth P-wave velocity model of the subsurface. A smooth velocity model is also needed in reflection processing for statics and migration. The unknown velocity distribution is related to the observed travel time through the ray path (Equation 1; Everett, 2013). The ray path depends on the unknown velocity, thus adding a high degree of non-linearity to the tomographic problem. The subsurface is divided into a grid where each cell is populated with an initial velocity to simplify the problem (Everett, 2013). Slowness (inverse velocity) is calculated, and then initial ray paths are determined. Modeled travel time from the initial ray paths are determined and compared to the observed travel times. These differences are used to update the starting model, and the process is iterated until the difference between the modeled and observed travel times is an acceptable range (for this study under 5 ms).

$$t = \int_S \frac{1}{v(x,y,z)} ds$$

Equation 1: Travel Time Relation to Velocity
t = travel time; S =ray path; v(x,y,z) = velocity

3.1 First Arrival Picking

The first arrivals were picked on shot gathers that had limited processing since processing changes the wavelet (Figure 14a). As a consequence of processing, the determination of arrival times associated with the phase of the wavelet will be biased, leading to distortions of the velocity model. Trace DC removal and an Ormsby bandpass filter (15-30-90-120 Hz) were used after testing different frequencies. The filter limited some of the low and high-frequency noise that was overpowering the first arrivals. Automatic gain control (AGC, length 400 ms) was also

used to boost the amplitudes of the first arrivals relative to the higher amplitude reflections. 400 ms was chosen based on testing different lengths and displayed the first arrivals the best. Before picking, the polarity of the trace was reversed such that peaks become troughs. The source created false first arrivals since it is a mechanical source (Figure 14b). As the piston accelerates into the foot plate, it produces an upward force on the truck which is then transmitted into the ground producing a seismic wave. The real first arrivals intersect zero time at the shot point while the false precursor intersects at negative times (Figure 14b).

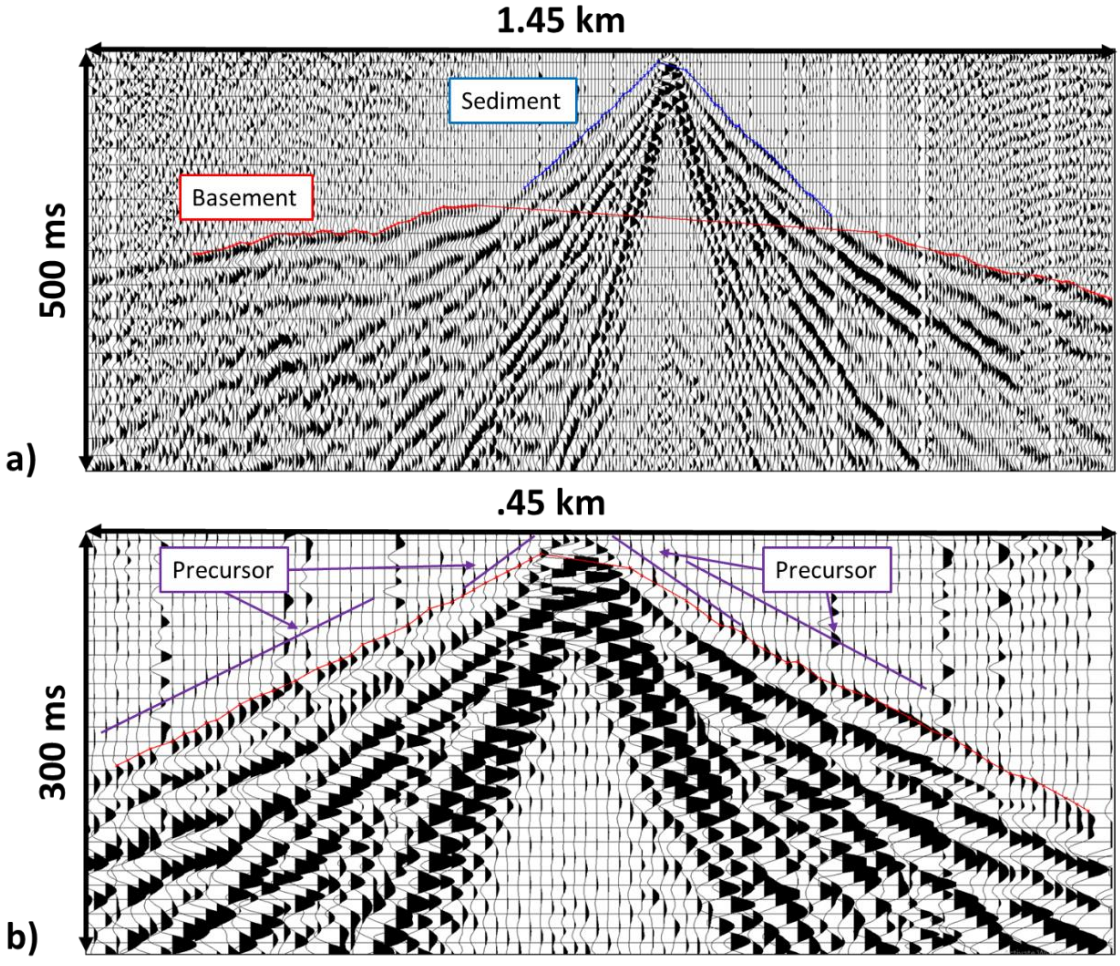

Figure 14: First Arrival Picking
Shot gather 20815 shows the example of the first arrival picks from sediments (blue) and Precambrian basement (red, a). The false precurser created by the piston firing are noticeable in b.

The first arrivals were picked in two groups: sediments and basement (Figure 14a). First arrivals were distinguished based on the change in the slope and the velocities as mentioned in the raw data section. All the shot locations were used, but for locations that had different days of shooting, only the second day was utilized. 18,263 sediment and 16,104 basement arrivals were picked (Figure 15). There is a clear break in slope representing the change in velocity between the basement and sediments.

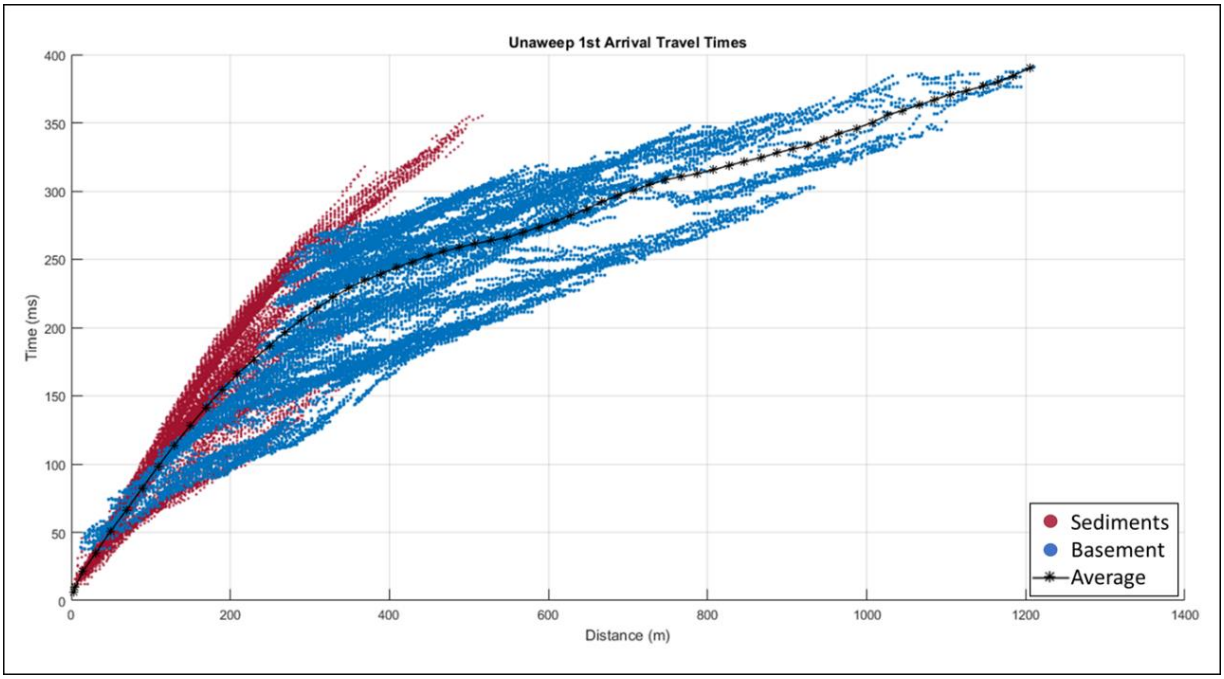

Figure 15: First Arrivals
The plot of all the first arrivals picked from the data, sediments in red and basement in blue. The black line represents an averaged travel time curve. A break in slope can be seen portraying the change from sediments to the basement.

3.2 CMP Sorting and 1D Velocity Inversion

Seismic tomography requires an initial model. In the case of complex structures, the initial model should already contain the large-scale structure of the velocity distribution to avoid being trapped in a local minimum (Everett, 2013). However, there is always the danger that the

choice of the starting model biases the final model. If, on the other hand, too simple of a starting model is used, the final result can converge on an unrealistic solution. A simple depth-dependent starting model is used in Figure 16 resulting in velocities over 7000 m/s which is unrealistic given the geology of the area.

To obtain an unbiased yet data-based and geologically plausible initial model, CMP-sorting of the picked travel times was performed. The arrivals were sorted into 12 common mid-point sections of 200 m width to derive representative 1D travel time curves. Sorting and inverting the arrivals into CMP bins allows for a first rough regionalization of the data, leading to a very smooth and robust 2D velocity model (Behm et al., 2007).

For each CMP bin, a 1D travel time curve is created from averaging the travel times in that bin within offset classes. This curve is inverted to get a 1D velocity model (example Figure 17) representative of the CMP location. The 1D velocity models were then combined to create a 2D starting velocity model for the 3D first arrival tomography (Figure 18). Dr. Michael Behm then took the 2D starting model and ran a 3D tomography program (Hole, 1992) to create the final travel time tomography model (Figure 19). The final model had nine iterations and an RMS error of 3 ms.

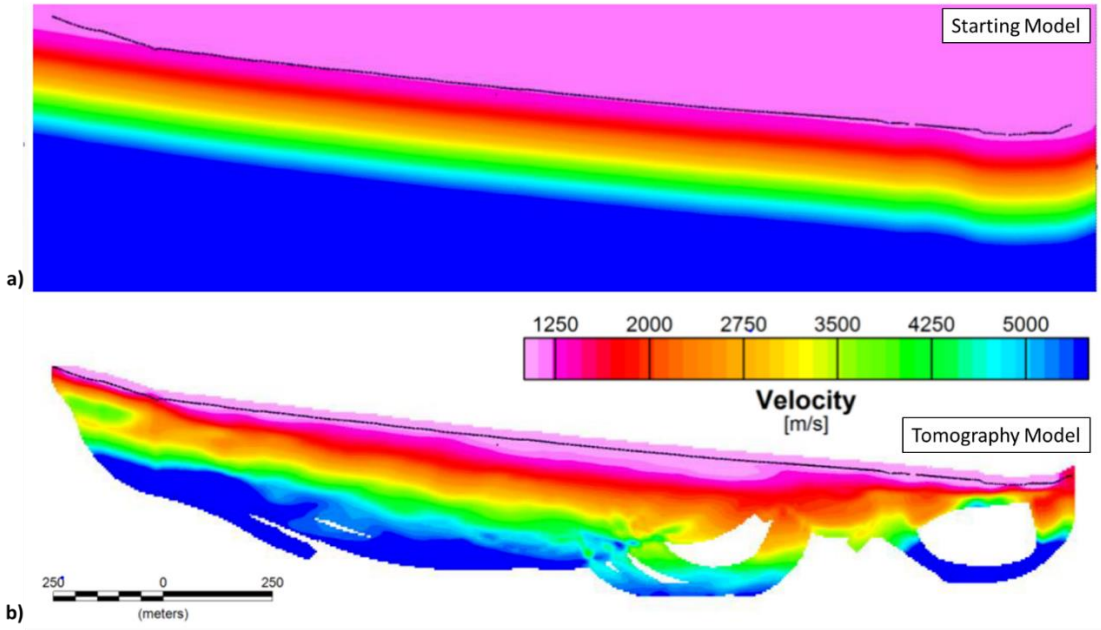

Figure 16: Non-geologic Tomography Starting Model and Results
First arrival tomography model using a single gradient velocity starting model (a). The tomography model (b) has velocities higher than 7000 m/s which is unrealistic given the geology of the area.

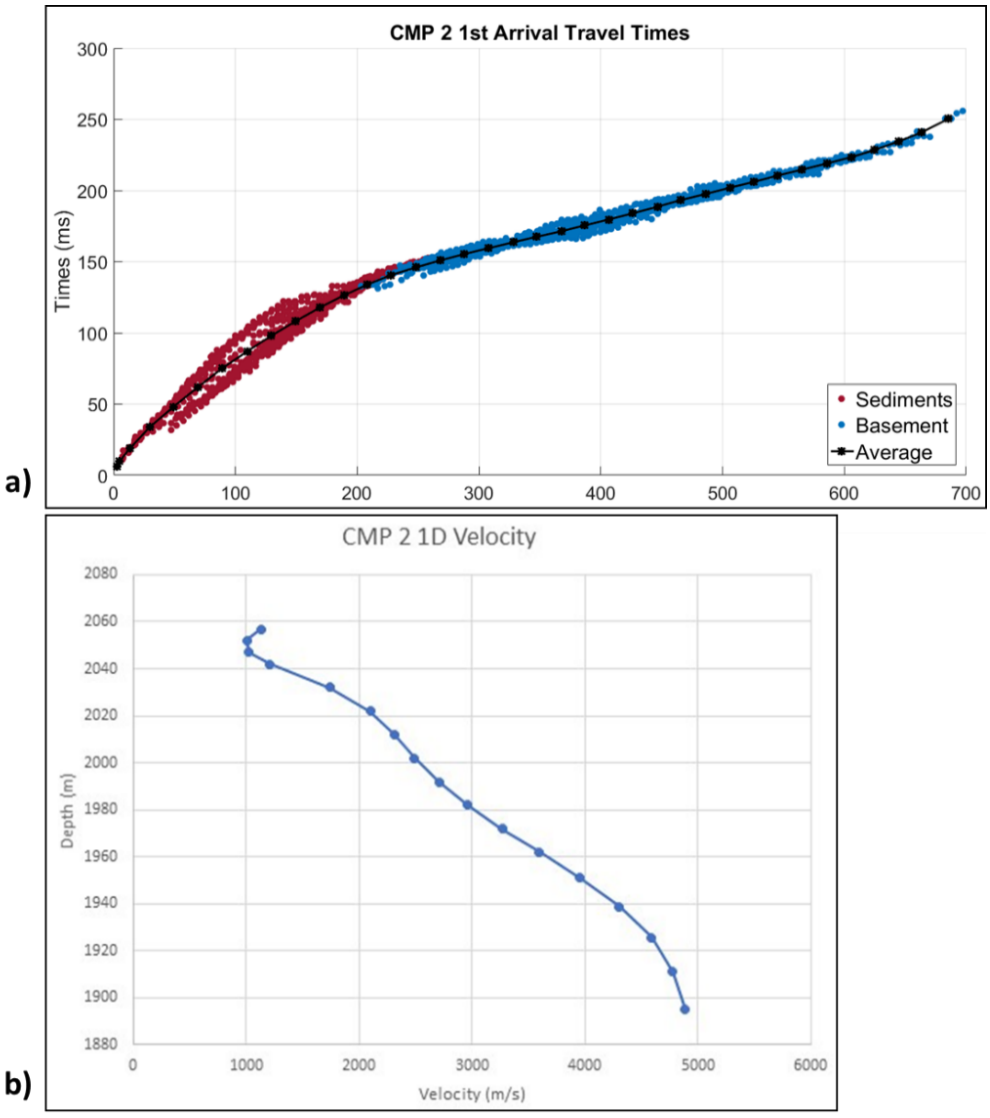

Figure 17: Example of CMP-sorted first arrival times and the inverted 1D Velocity Model First arrivals from CMP 2 (a) displaying a clear break in slope between the sediment and basement velocities. The inverted 1D velocity from CMP 2 (b) shows the smooth velocity. The small velocity inversion near 2050 m is due to the inversion process.

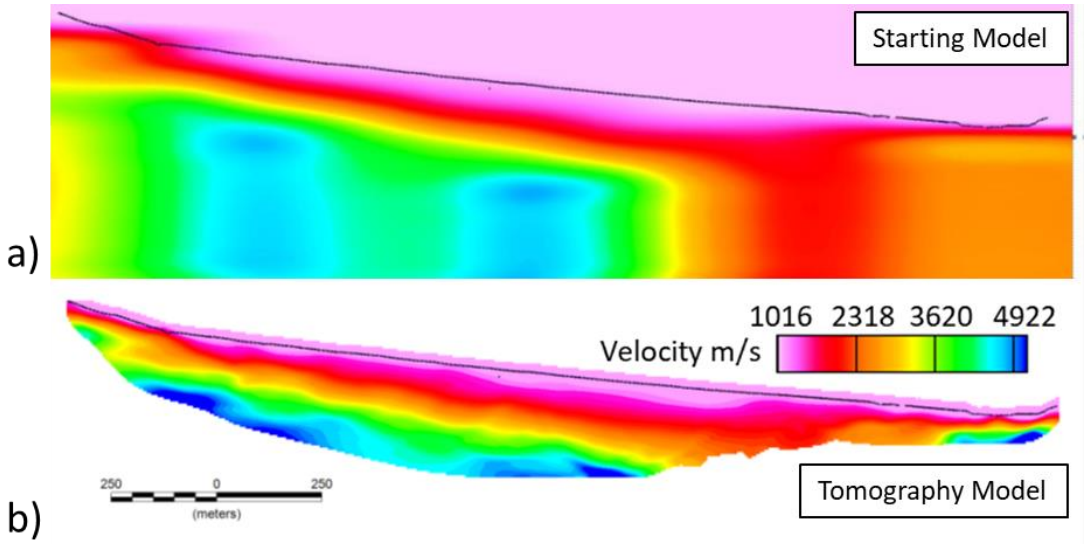

Figure 18: 2D starting model (a) and resulting final model (b) of the 3D tomographic inversion. The starting model displays no fast velocities in the southern portion.

3.3 3D Tomographic Model

The final tomographic model shows a range of velocities from 1000 m/s to just over 5000 m/s (Figure 19). The results represent a smooth velocity model of the subsurface such that velocity contrasts are smeared. The velocity jump from sediments to metamorphic Precambrian basement is not represented by a sharp contrast. From the first arrivals, the Precambrian basement is around 4000 m/s and faster, so the faster velocities in Figure 19 are estimated to be the Precambrian basement. 3000 m/s was chosen instead of the 4000 m/s seen in the first arrivals because a delay time model for the Precambrian basement converged around 3000 m/s isoline in the tomography model (Behm et al., 2019). High velocities do not occur in the southern segment of the model indicating an over-deepening of the Precambrian basement in this region. If the basement is significantly over-deepened here, the steep walls of the Precambrian basement will cause the rays to bend downwards and not come up again. This is evident in shot gather at 1605

m, first arrivals from the sediments are present but not the Precambrian basement (Figure 20). The first arrival tomographic model suggests over-deepening of the Precambrian basement but does not indicate the geometry.

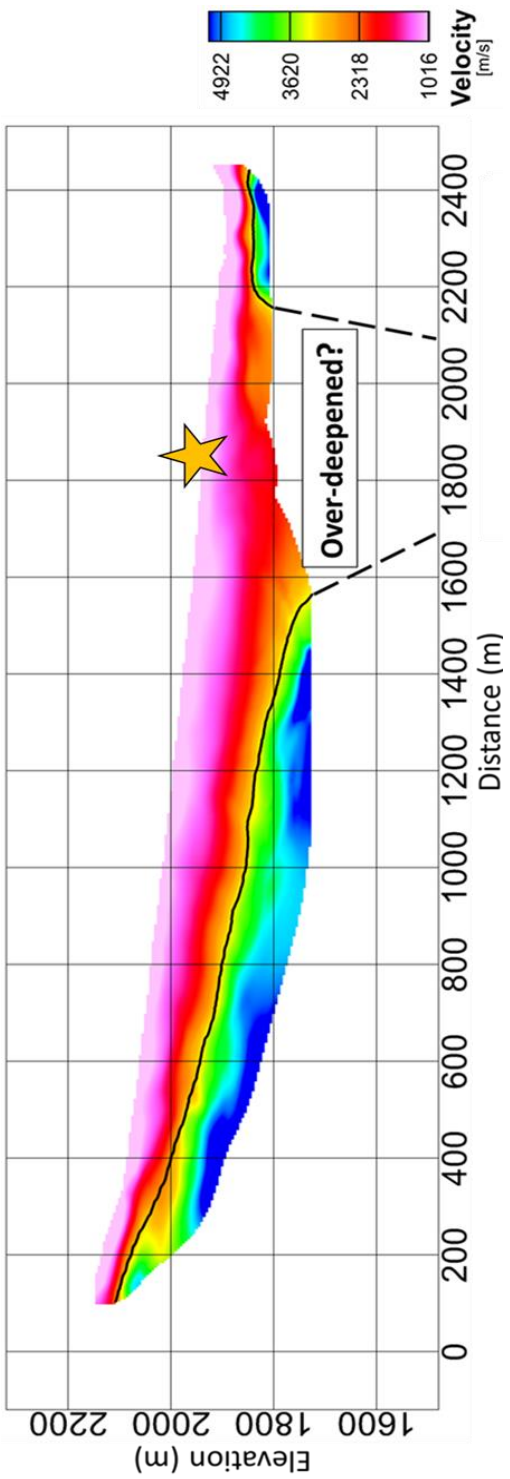

Figure 19: First Arrival Tomography Model
Results from the first-arrival tomography express an absence of faster velocities in the area hypothesized to be over-deepening. The basement is interpreted to be around the isoline of 3000 m/s (yellow). The location of the shot gather in Figure 27 is marked with a star. Modified from Behm et al. (2019).

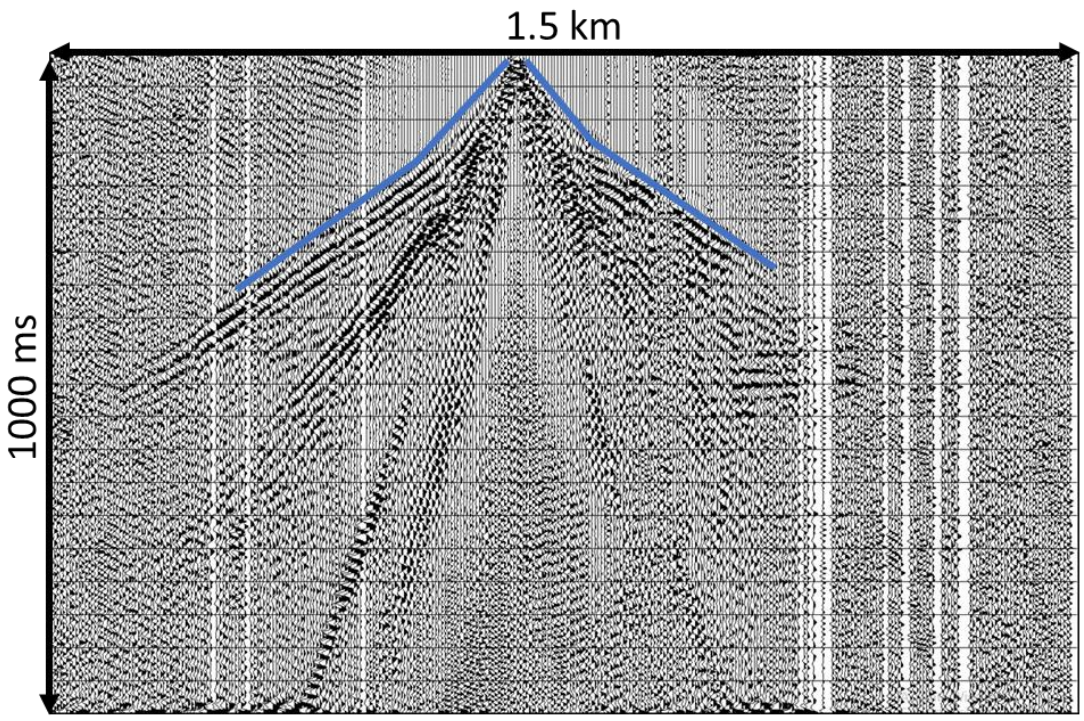

Figure 20: South Side Shot Gather
Shot gather 21605 shows the first arrivals of the sediments (blue). Due to the complex geometry of the basement, no arrivals are present from the Precambrian basement.

Chapter 4: Reflection Processing

Reflection processing was done using the software ProMAX (Landmark Haliburton). Most of the processing was done in Vienna, Austria at the University of Technology with the help of Dr. Werner Chwatal. A typical 2D seismic processing workflow was applied (e.g.Yilmaz, 2001; Figure 21). Images of processing flows used, and parameters are located in Appendix A. Description of seismic fundamentals and standard processing sequences follow textbooks by Yilmaz (2001), Sheriff and Geldart (1995), and Hart (2010).

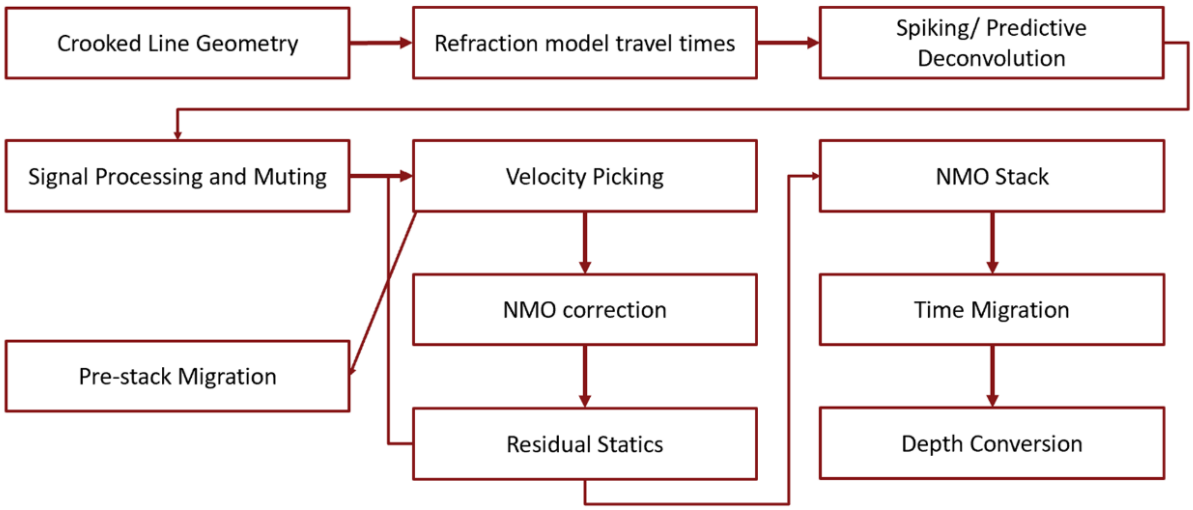

Figure 21: Processing Flow
Processing flow used for this study. Velocity picking through residual statics is an iterative process.

4.1 Geometry

The first step of geometry is determining that shots and receivers are in the right location along the 2D line. The data is then sorted into CMP gathers which changes the geometric reference system of the survey from shot-receiver coordinates to mid-point (CMP) - offset coordinates. The mid-point is determined by the halfway point between the shot-receiver pair. In the real geometry, all shot-receiver pairs will not have the same mid-point (CMP), so binning is

needed to sort the CMPs into a common CMP gather. Next CMP binning is applied. The profile is broken down into bins of equal width, and if a CMP of a source and receiver pair fall within a bin, it is assigned to that bin. The CMPs that falls into each bin are combined into a CMP gather and are NMO corrected, and then are stacked together. The resulting trace is assigned to a nominal CMP at the center of the CMP bin. Each trace imaged in the final stacked images represents one nominal CMP located in the center of a CMP bin. The number of traces stacked in a bin is called the fold. Higher fold means a higher signal to noise ratio because as traces are stacked together, the random noise is subdued or eliminated while the signal is amplified.

For this survey, crooked line geometry was applied. The line has a noticeable bend since acquisition followed the 4x4 road to use the truck-mounted source. Next CMPs were determined for all shot-receiver pairs (Figure 22). The CMP bins of 2.5 m were chosen based on the receiver distance of 5 m. The traces are then assigned to a nominal CMP location at the center of each bin. The nominal CMP locations follow the same line geometry determined from the location of the shot and receivers from acquisition (Figure 22). The number of traces in each bin is represented by the fold (Figure 23). The highest fold is located in the center of the line (Figure 23). The fold displayed is not the final fold of the line, during signal processing noisy traces are eliminated, lowering the fold. When stacking the data, only a specific offset range is used which further reduces the fold. However, the highest fold (150-300) remains near the center of the line where previous studies show a thick sediment fill.

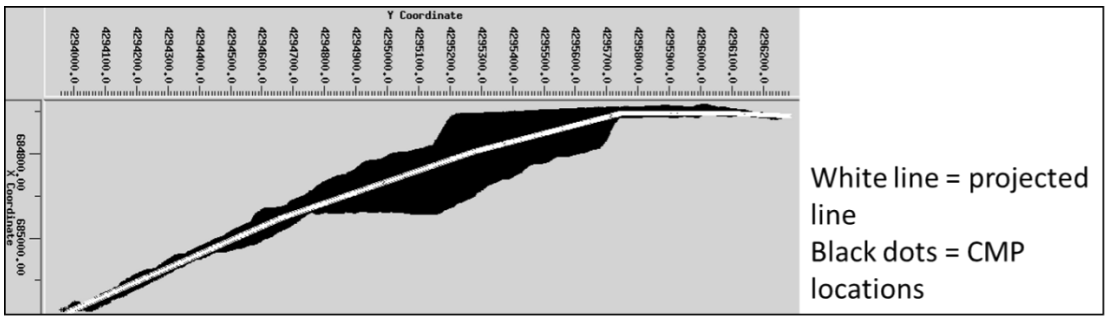

Figure 22: Line Geometry and CMP Locations
The crooked line geometry that the line will be processed in. The black dots represent individual CMP locations. Those locations are binned and then projected to a single location in the center of each bin represented by the white line.

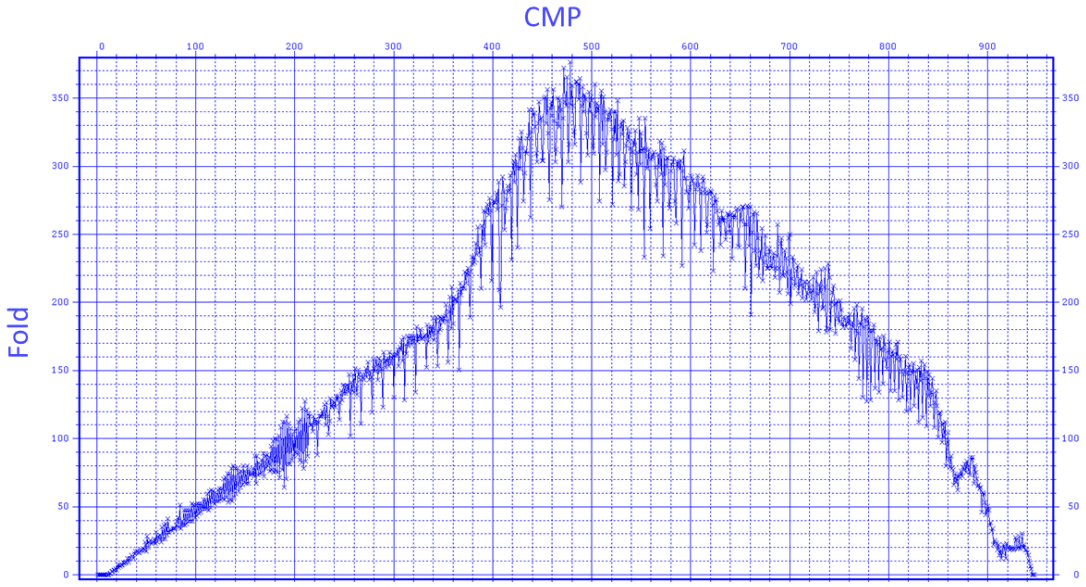

Figure 23: Fold Map
The fold for each CMP. The higher fold is seen in the southern portion of the line because the source spacing was 5 m instead of 10 m.

4.2 Signal Processing

The goal of signal processing is to align reflections better through the use of statics, suppress non-reflection energy by trace killing and muting, and to increase resolution through deconvolution. The results should be data with a higher signal to noise ratio and with data consisting of reflections and little background noise (Figure 24).

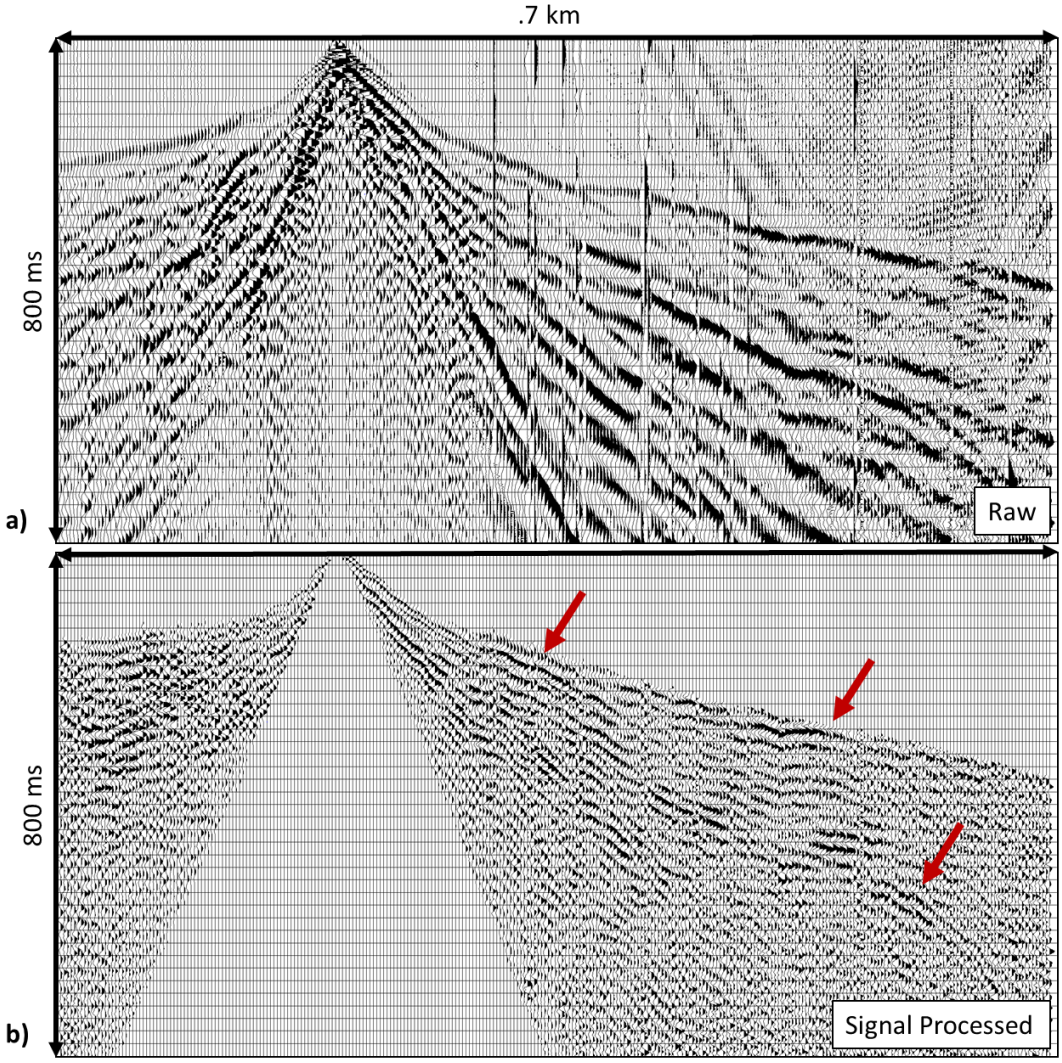

Figure 24: Before and After Signal Processing
The difference between the raw shot gather (a) and the results of signal processing (b). The goal of signal processing is to increase the signal to noise ratio and to be left with only reflections to process. Reflections that are visible after signal processing are highlighted by the red arrows.

Elevation and Refraction Statics

Long wavelength differences in the elevation between shots and receivers will be overprinted on the data causing false structures that mimic the topography. Short wavelength differences create inconsistency that will lower the resolution during stacking. Statics create time shift that account for these differences and add coherency to traces before stacking. There was variable elevation along the line (Figure 13). Elevation statics bring shot and receiver locations within a CMP gather to a common datum to account for changes in elevation between the locations. A replacement velocity is used to calculate the time shift to bring the source and receiver locations to the same floating datum. In this survey, a floating datum was used with a replacement velocity of 1250 m/s. A replacement velocity of 1250 m/s represents the average velocity of the near offset sediment first arrivals. The results will be shifted to the final datum to present the results in elevation after depth conversion.

The first few meters of the subsurface consists of the weathering zone which is a low-velocity zone that can vary in velocities and depth both laterally and horizontally. The variation can cause time shifts in the traces, limiting resolution due to misalignment. Refraction statics calculates the time shifts and applies it to the data. A velocity of the weathering layer (v_0) is assumed to be 800 m/s. The first arrivals of the first 4-8 traces on each side of the shot point in the CMP shot gathers were re-picked. Near offsets (less than 25 m) are used to represent the refractor below the weathering layer. The first arrivals were picked using a mean automatic gain control (AGC) with a length of 100 ms and trace dc removal. A delay time model of the refractor below the weathering layer was calculated, this includes the refractor travel time (delay time) and the velocity of the consolidated material (Telford et al., 1990). The delay times are then converted to depth to represent the depth of the consolidated material which equals the thickness

of the weathering zone. The delay time model substitutes the variable weathering zone with the consolidated material. The substitution results in a time shift calculated from the differences between the two velocities (weathering layer and consolidated layer). The time shifts (refraction statics) are applied to the traces. Total static corrections include elevation, refraction, and residual (calculated after the velocity analysis).

Deconvolution

The convolution model is a concept that describes how the seismic source wavelet, the geologic structure, and noise contribute to the observed recording at a geophone (seismic trace) (Figure 25). Each subsurface layer has an individual impedance based on the properties of the layer. The reflection coefficient of each impedance boundary depends on the impedances of the layers above. The reflectivity series represents the sequence of all reflection coefficients vs. depth or converted two-way time. The reflectivity series is convolved with the seismic source wavelet, and noise is added. The seismic source wavelet represents the seismic source signature as it would be recorded directly at the source. The phase of the data is also contained within the wavelet. The phase of the data represents the time delay of where the peak energy falls. The broader the bandwidth of frequencies of the seismic data, the closer the wavelet is to a spike with little side lobe energy. This is the ideal wavelet since it gives the highest resolution. The goal of deconvolution is to increase the resolution of the data by removing the convolutional effect of the band-limited source wavelet.

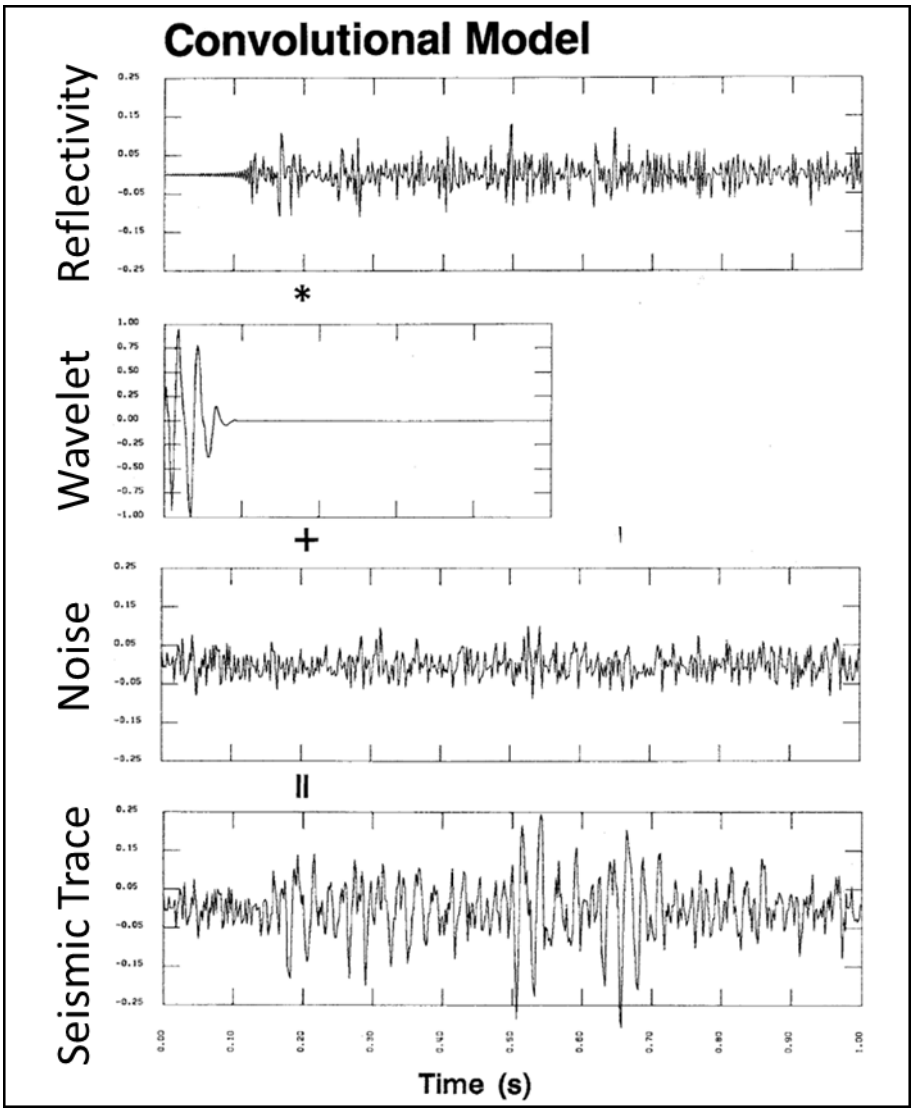

Figure 25: Convolutional Model
Modified from Yilmaz (2001) shows how the convolutional model is used to create the seismic trace. The seismic wavelet is convolved with the reflectivity of the subsurface and noise is added to create the seismic trace.

Spiking/predictive deconvolution was used to process the data. Spiking deconvolution attempts to determine the Earth's natural filter and then remove it. As the source wavelet goes into the subsurface, the Earth can be considered as a low-frequency filter that attenuates the high-frequency components. The filter narrows the bandwidth of the wavelet and results in lower resolution. By removing this filter, spiking deconvolution aims to restore the high-frequency signal in the data. Boosting the high frequencies broadens the bandwidth, narrowing the wavelet and increasing resolution. Narrowing of the wavelet is essential to improve the vertical resolution in the data.

Predictive deconvolution is used to remove predictable noise from the seismic image. Predictive deconvolution helps to limit noise that was repetitive through the acquisition like power lines and helps predict and eliminate any multiples within the survey. A minimum phase predictive filter was used with a length of 100 ms. 100 ms of the trace was examined to find any repeating patterns, and if these were repeated throughout the trace, then it was assumed to be noise and removed. 100 ms was chosen to find repetitive noise that is displayed within the whole trace and was determined based on testing different lengths. A bandpass filter of 30-40-140-180 was applied after deconvolution to limit the effects caused by boosting the low and high frequencies during spiking deconvolution. This filter was chosen after testing different frequencies to see which ones removed the added noise but left the wanted signal. A comparison of data before and after deconvolution can be seen in Figure 26. The low-frequency noise is reduced, and more high-frequency reflections are visible in the data.

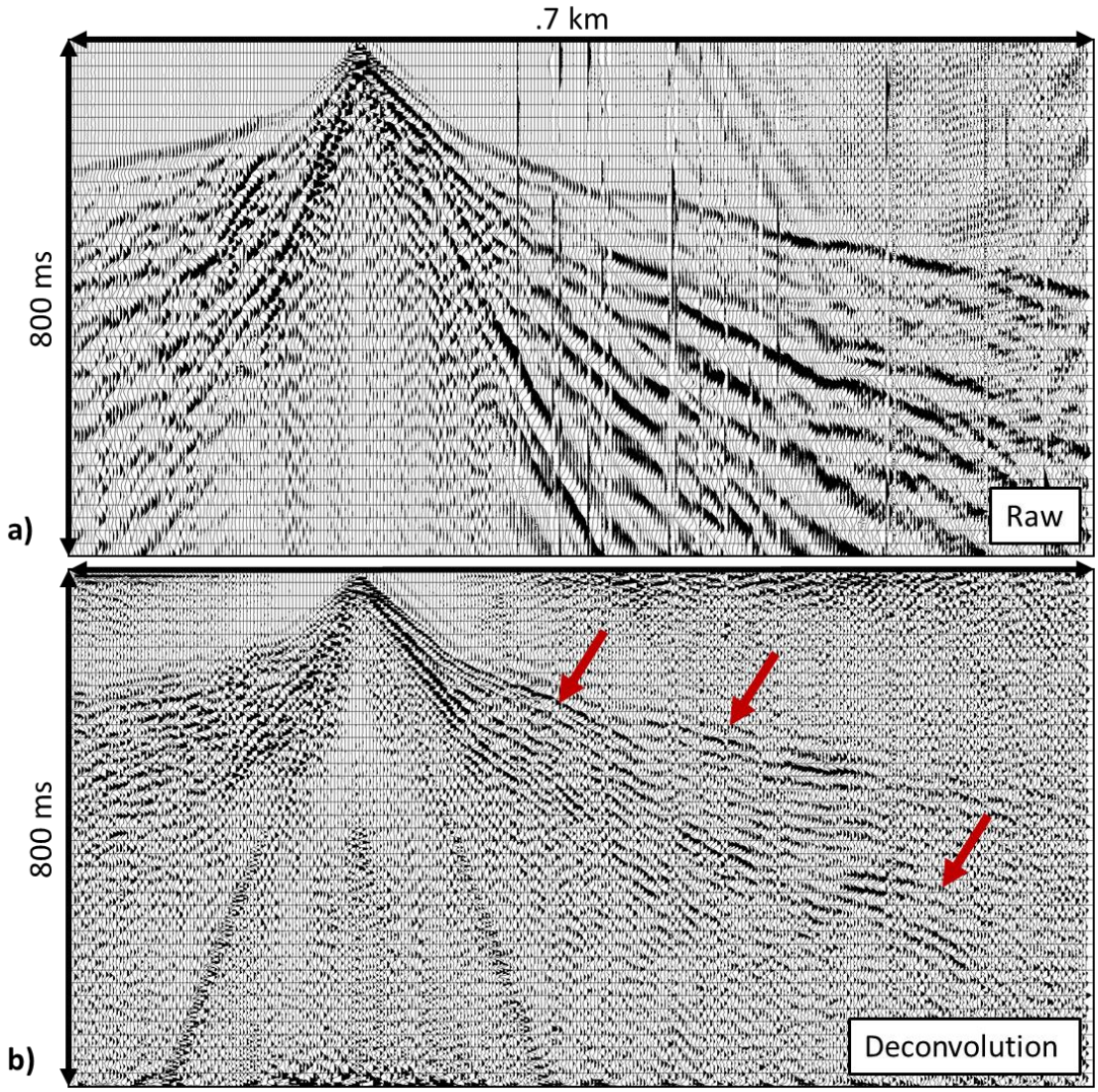

Figure 26: Before and After Deconvolution
Deconvolution's goal is to narrow the wavelet to increase resolution and to increase the signal to noise ratio. Before deconvolution (a), the data is low resolution and noise is more apparent. After deconvolution (b), the events appear higher frequency and reflections are seen over the noise. Reflections that are visible after deconvolution are highlighted by the red arrows.

Trace Killing and Muting

Trace killing is used to eliminate traces with low S/N ratio or simultaneous shots recorded within each shot record. Traces that were killed include noise from the truck or footprints (Figure 27a). At the beginning of the survey, both sledgehammer and impact source shots were being conducted at the same time, and some of the shot gathers reflect this (Figure 27b).

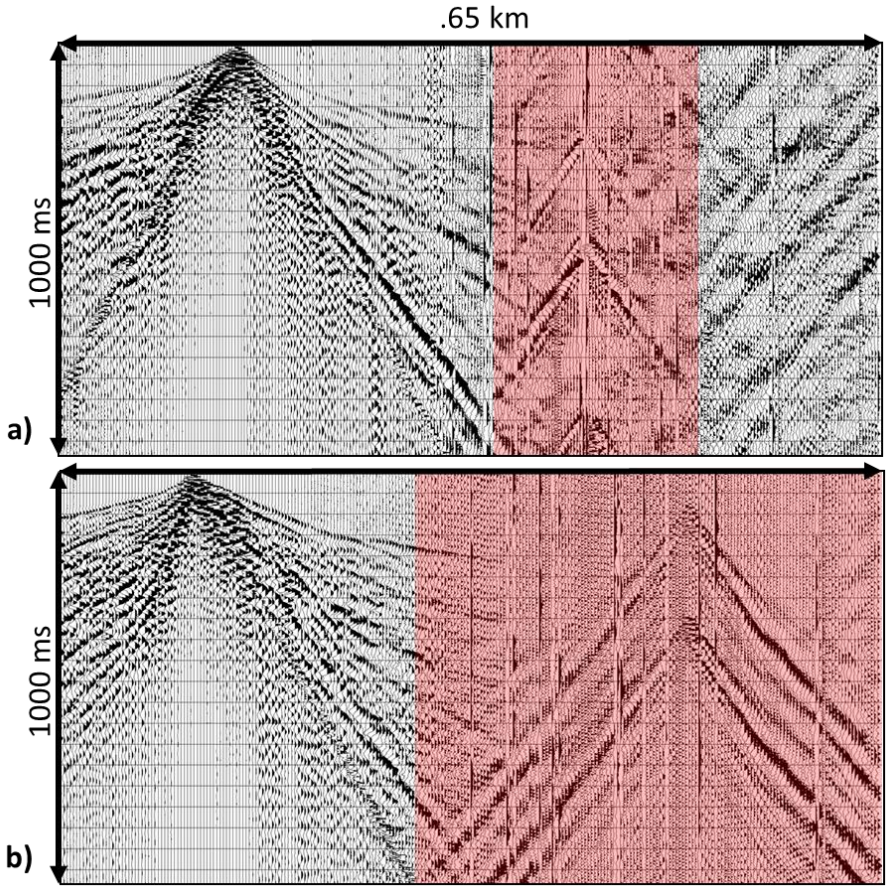

Figure 27: Trace Kill Examples
The red represents traces that were cut out of the data due to the low signal to noise ratio.

Muting involves removing signals within the data that are not reflections, so they are not stacked into the data. If left in they can influence the final results creating false events. Muting removes the part of the trace indicated. Both ground roll and refractions are the unwanted signals

in reflection processing. First arrivals are removed in a top mute; this also removes any noise present in the gather before the first arrivals. Ground roll is removed with a bottom mute. Since muting removes the entire portion of trace indicated, reflections that arrive the same time as the ground roll will also be removed. Ground roll has a high amplitude, and it is difficult to separate the ground roll from the wanted reflections if they arrive at the same time. A top and bottom mute are created for each shot gather so that only the unwanted signal is removed (Figure 28). Muting is done after statics and deconvolution. Final signal processed results are seen in Figure 24.

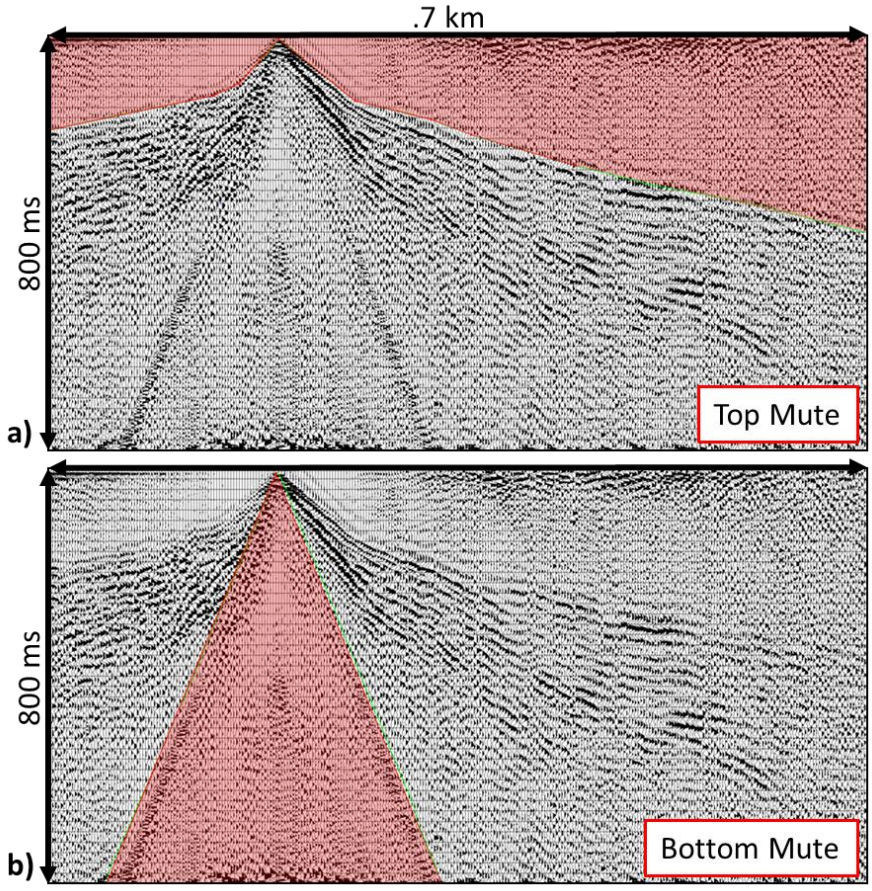

Figure 28: Top and Bottom Mute
The red represents mute that is applied to the data to remove the first arrivals (a) and ground roll (b).

4.3 Velocity and NMO

After signal processing, mostly true reflections should be left plus some leftover noise. The shot gathers are sorted into common midpoint gathers (CMP-gathers). A CMP gather represents one reflection point in the subsurface, and the curvature of the reflections can be described by hyperbolic moveout which depends on the subsurface velocity (Equation 2). The hyperbolic moveout needs to be removed to allow stacking. The moveout is corrected by determining a stacking velocity and applying normal moveout (NMO) correction. Stacking velocity represents an average velocity along the ray path to the reflection point. If the stacking velocity is incorrect, the different offsets of the reflector will not align horizontally, lowering the resolution of the trace. Velocities from individual layers (interval velocity) are determined from the stacking velocities (Equation 3).

$$t = \sqrt{t_0^2 + \frac{h^2}{V_{NMO}^2}}$$

Equation 2: Normal Moveout (NMO)
t = travel time at offset; h = offset; t_0 = travel time at 0 offset; V_{NMO} = stacking velocity

$$V_{int} = \sqrt{\frac{t_2 V_{NMO2}^2 - t_1 V_{NMO1}^2}{t_2 - t_1}}$$

Equation 3: Dix Equation
V_{int} = interval velocity of layer; t_1 = two-way travel time to top of layer; t_2 = two-way travel time to the bottom of layer 2; V_{NMO1} = stacking velocity at the top of the layer; V_{NMO2} = stacking at bottom of layer

Velocity Analysis

Stacking velocity is needed for NMO corrections. CMP gathers are grouped into super gathers. The supergather increment of 25 was used, meaning every 25 m of the line represented a single super gather and included 11 individual CMP gathers. Velocity analysis precompute process in ProMAX was then used to create velocity plots (Figure 29). The semblance plot is located on the left and represents the stacked amplitudes for different velocities. Semblance values are large for coherent events. Next to the semblance plot is the NMO-corrected supergather for the picked velocity model. The flattening of the reflectors can be checked to ensure the correct velocity is being picked. The next panel represents the supergather stack for the velocity function chosen. The right panel represents stacks using different velocity functions. The velocity functions are represented by the black lines in the semblance plot. The velocities picked are interpretations made by the processor based on the data available. Different processors will have different interpretations of the velocity.

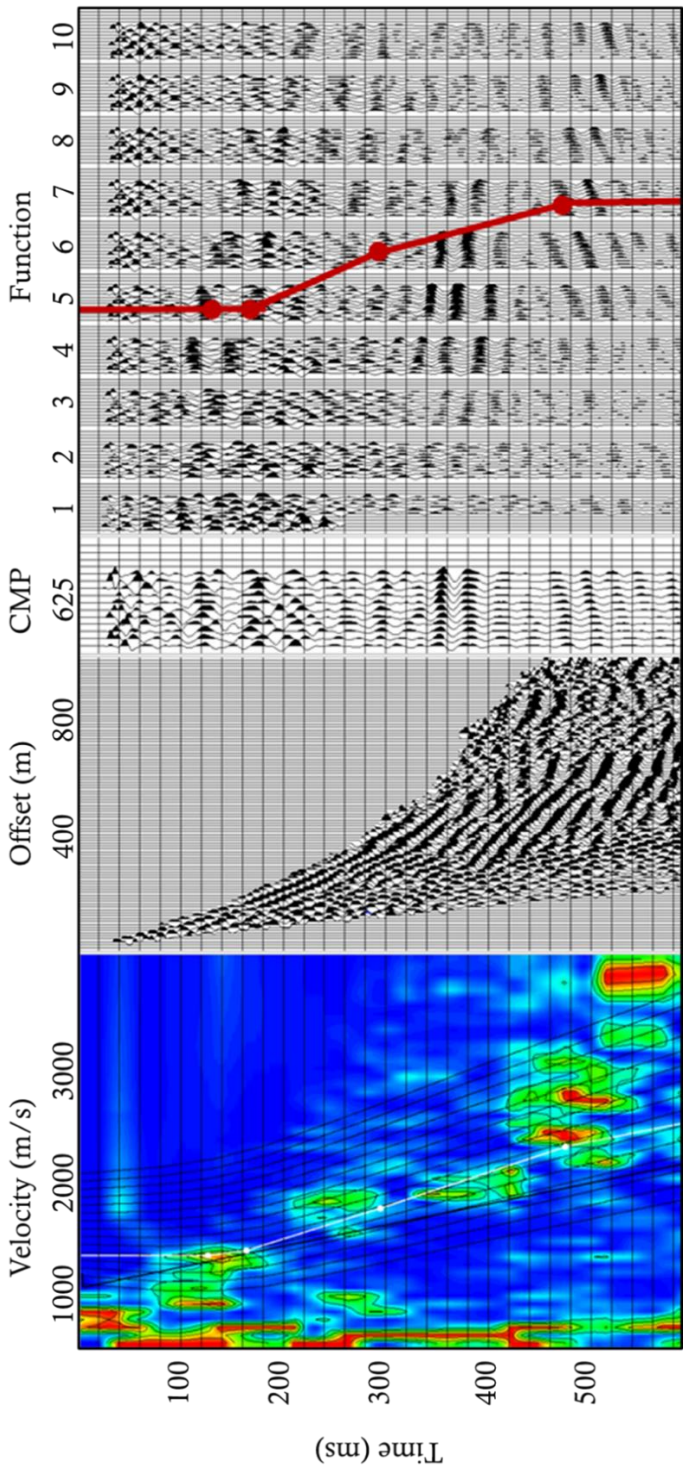

Figure 29: Velocity Analysis
The panel used to pick velocities including semblance plot, NMO corrected gather, CMP stack, and plots with CMP stacks. Different velocity models appear as black lines in the semblance plots. The red line represents the velocity model picked from the data.

The velocities for each super gather were picked mainly using the right panel. The semblance plots for this data were noisy due to the noise left in the data, and were unreliable. Care was also taken not to pick multiples that could be seen above and below the strongest events. The southern portion of the line showed the presence of three individual events in the super gathers while the northern portion only showed one. An example of the velocity picking for the southern portion is shown in Figure 29. Different interpretations of velocity can be made that fit the data, but the velocity structure would remain largely the same. After the velocity is picked, then the velocity is used to NMO correct the gathers.

Residual Statics

After the NMO corrections are applied to the gathers, residual statics can be determined. Residual statics account for time differences caused by differences in the weathering layer that were not caught in the original static calculation. Time differences in the traces can lead to smearing when the traces are stacked which can lead to lower frequency horizons or even multiple events when there are supposed to be one. A reference horizon is picked on the NMO stack. Then traces in each CMP are separated, and time differences of the reflector in the individual traces to the reference horizon are estimated. Taking all CMPs into account, these time differences can be inverted for surface-consistent residual statics at the source and receiver locations. These statics are applied to the traces, and NMO-correction and the gathers are stacked. The process is iterated until there is little difference between the current residual static corrections and the previous iteration.

Constant Velocity Stacks

After two iterations of residual statics, no further improvement was gained. Looking through the CMP stack, it was noticeable that the first layer did not image well especially on the northern portion of the survey. Constant velocity stacks were created to test which horizons are visible for specific velocities. Instead of a velocity model being used to NMO correct and stack the data only a single velocity is used for all the data, so only the layer with the stacking velocity used will be resolved. The constant velocity stacks were used to help determine the velocity of the first layer since the picked velocity model had a hard time resolving the northern portion of the survey. Looking at the different constant velocity stacks, the velocity that the first layer is most visible at is 1300 m/s (Figure 30). Since it was clear the first layer needed to be corrected using 1300 m/s, two picks at 1300 m/s were made for the first layer in each supergather.

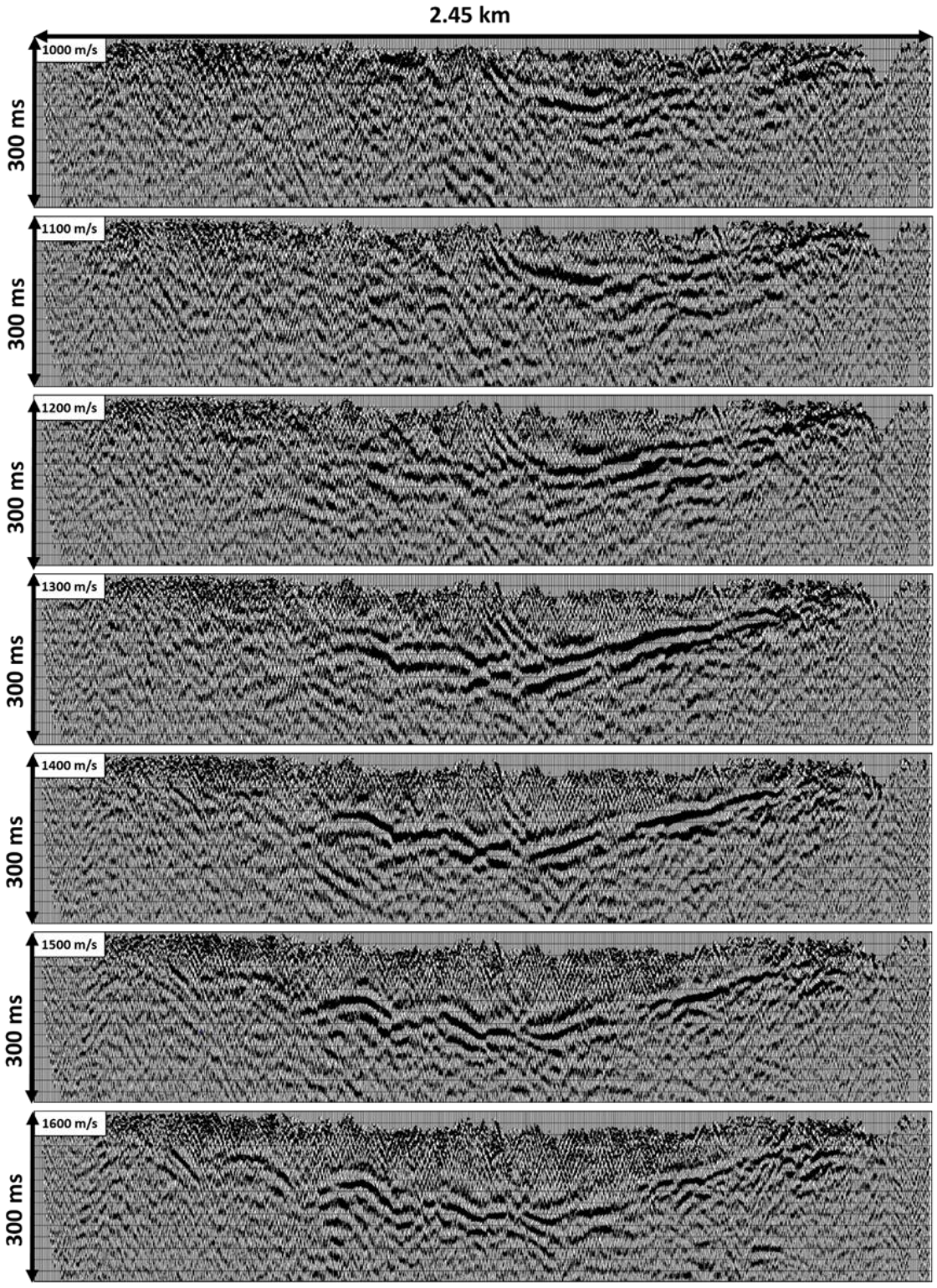

Figure 30: Constant Velocity Stacks
Constant velocity stacks ranging from 1000 m/s to 1600 m/s in 100 m/s increments. The first horizon has the strongest amplitudes and lateral consistency in the 1300 m/s stack.

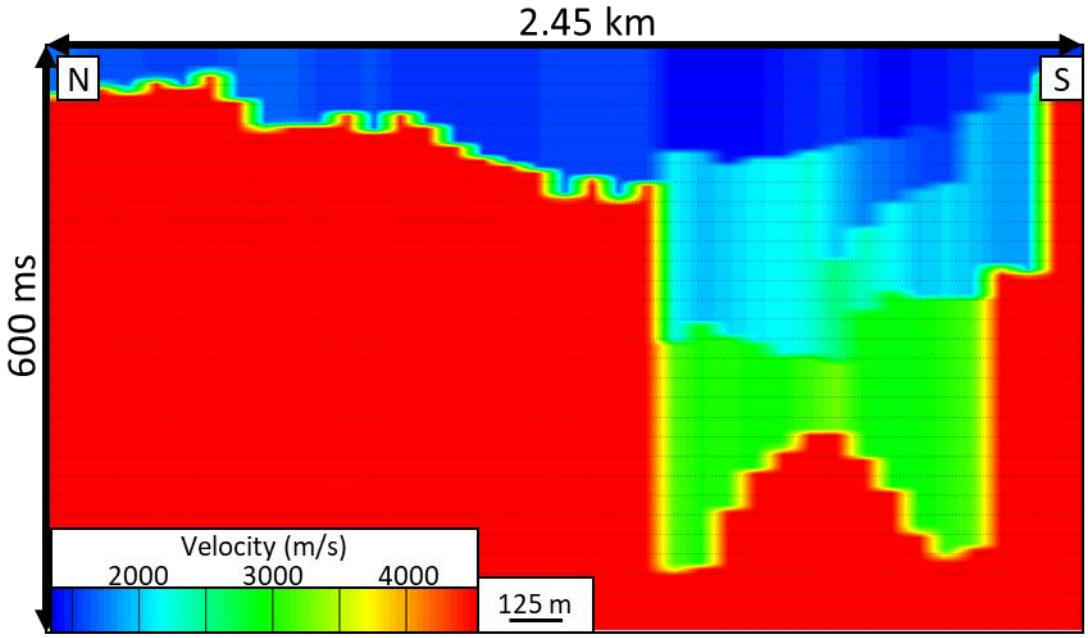

Figure 31: Original Velocity Model
Velocity model determined through the velocity picking. Steep sides of the basement are indicated by the rapid drop of fast velocities. The anticlinal feature seen on the southern portion is due to the bow tie effect on imaging structures with U-shaped geometries.

CMP Stack

After the velocity has been picked from the velocity analysis (Figure 31), and the NMO corrections have been done the CMP stack is created. NMO corrections remove the hyperbolic moveout so reflections can be stacked to represent one single event in a single trace and coherent events become visible. After the corrections are applied a CMP stack can be created (Figure 32). Each CMP gather is stacked into a single trace and then placed in the correct location along the line. A mean coherency filter with a root power scalar of .5 was also applied to the stack. The filter was done to amplify coherent events throughout the data, increasing the signal to noise ratio since most noise is incoherent. CMP stacks may not show horizons in their correct location since migration has not been done. Figure 32 shows the CMP stack, and multiple horizons in the southern portion are visible.

Noticeable on the southern side of the image is what looks like a frown with two smaller frowns on either side creating a bowtie effect (Figure 32). The bowtie structure is commonly seen in syncline geometries in un-migrated seismic data (Figure 33). In CMP gathers the events theoretically represent a unique impedance boundary centered between the shot-receiver pair, but a complex structure can result in multiple events recorded at each receiver location (Figure 33).

A synclinal feature can record three individual events for each shot-receiver pair. Velocity analysis, NMO corrections, and CMP stacking are assuming the events are located at the mid-point and represent individual impedance boundaries. After these processes are done, the CMP stack will show three different horizons in different locations; this creates the bowtie effect (Figure 33). If the synclinal feature were a V-shape instead of a U, the waves from the source would bounce off the steep walls and lose energy before reaching the receivers (Figure 34). Only two instead of three individual events would be recorded by the receivers, eliminating the

anticlinal event in the middle of the bowtie feature. This anticlinal feature is visible in the CMP stack, meaning there is a U-shaped structure instead of a V-shape. The bowtie structure is commonly seen in Quaternary glacial valleys like in Northern Italy (Figure 33, de Franco et al., 2009). After the migration (Figure 33c) the bowtie structure becomes a clear U-shaped reflection. If the subsurface consisted of flat non-dipping layers, then the CMP stack would represent the geology and would be the final results, but complex layer geometry and velocity variations lead to features like the bowtie structure.

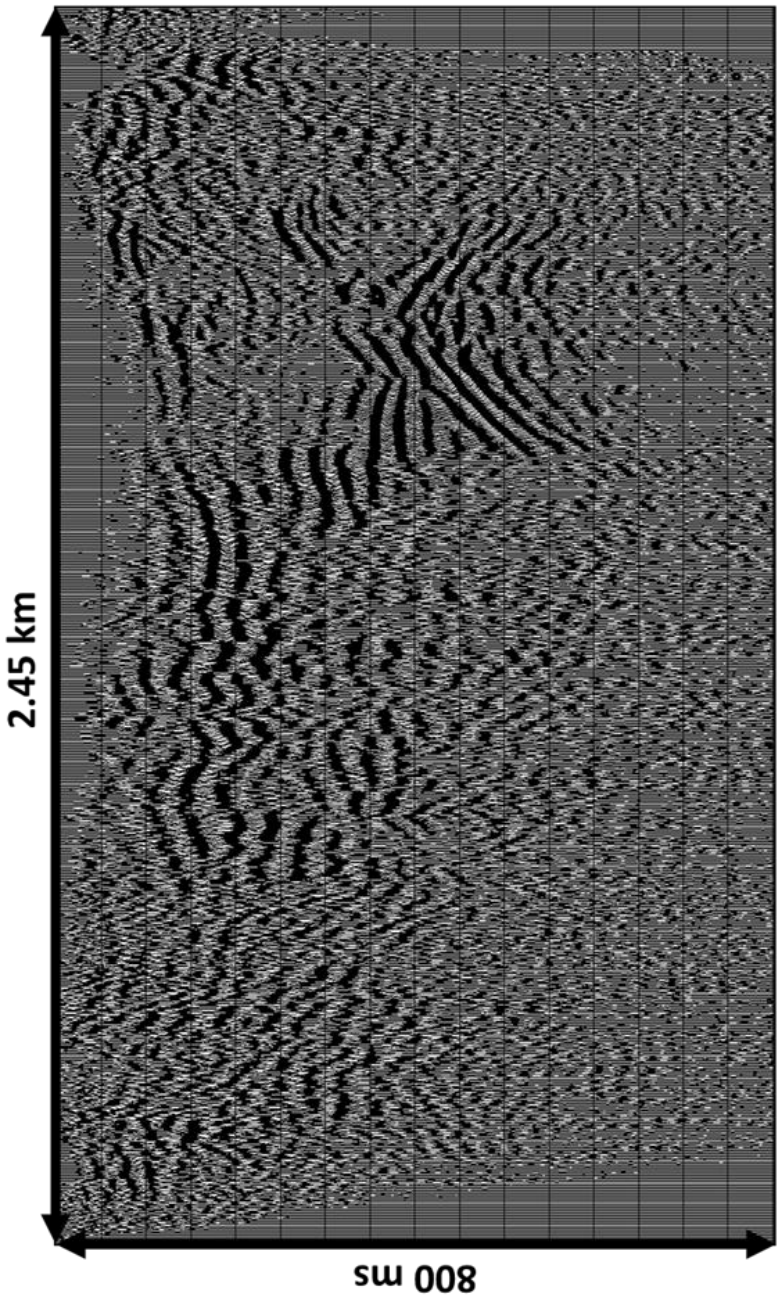

Figure 32: CMP Stack
The CMP stack is created from the NMO corrected CMP gathers. The data remain at the datum created during the statics. There is a noticeable bowtie structure in the lower southern portion that indicates an unmigrated U-shaped structure. The first layer does not have as strong of amplitudes as seen in the constant velocity stacks and is not as laterally continuous. The northern portion of the line does not display any clear events.

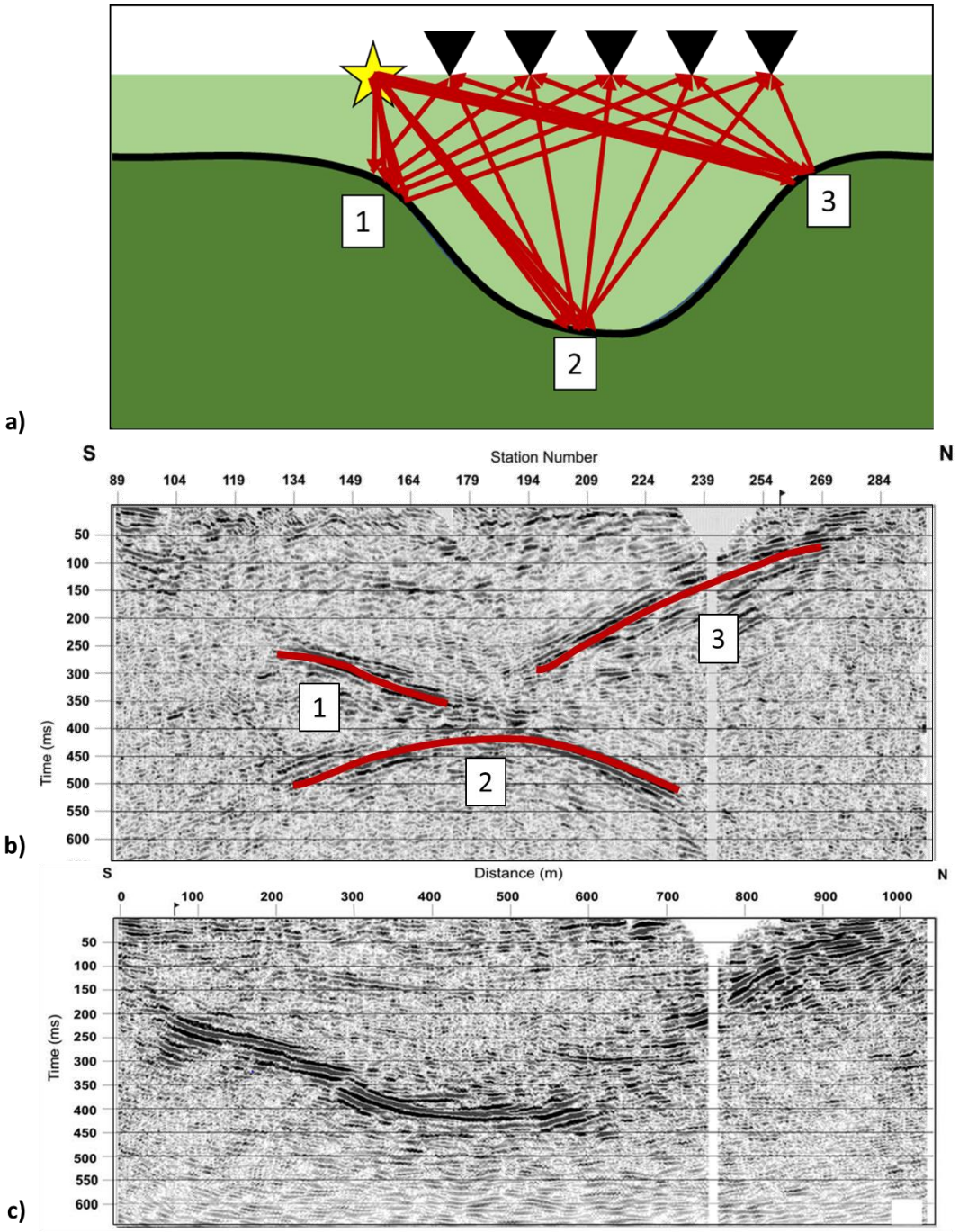

Figure 33: Synclinal Bowtie Geometry

U-shaped structures will create three individual reflection points within the structure due to changing dips (a). The results of the reflections points are displayed in the modified image by de Franco et al. (2009) (b). The three reflection points result in three reflections in the CMP stack resulting in a bowtie structure. Migration is needed to correct the bowtie and get an accurate model of the structure (c). De Franco et al. (2009) shows the results of a reflection seismic line taken across a glacial valley in Northern Italy (b and c).

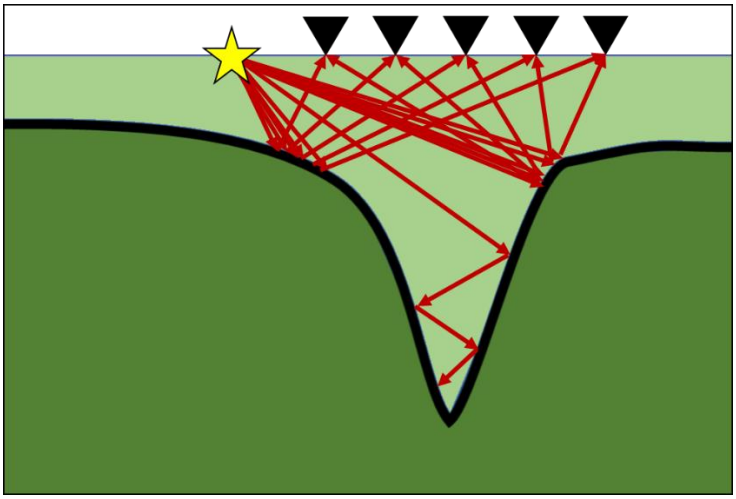

Figure 34: V-shaped Imaging Geometry
V-shaped structures will create two reflection points. The waves in the V-structure will reflect and refract off the steep dips and lose energy before reaching the surface and receivers.

Final Velocity Model

The velocity from the velocity picking results in the stacking velocity Figure 43. The model also clearly shows deep fast velocities in the southern portion, which match the Precambrian basement, and three distinct layers within the deeper southern portion. An anticlinal feature is apparent in the fast velocities of the southern end of the line. The feature reflects the unmigrated data creating the bowtie structure (Figure 33). If this velocity model were used to migrate the data, then the migration results would produce similar results as the CMP stack. To prevent this, the velocity was manually manipulated to flip the frown to invert the anticlinal feature (Figure 35). The velocity model represents a middle ground between a U and V-shaped geometry.

For a proper migration, a realistic velocity model of the subsurface is needed. An exact velocity model is not possible since that would mean the exact structure and layers of the subsurface are already known. Improving the velocity model using the known geology gives the

most accurate answer. Only the geology that is known should be used to modify the velocity model to prevent biasing the results. The final stacking velocity model that has geologic input and can be converted to interval velocity for migration (Figure 35). The model can be interpreted to represents a V or U shape geometry. Interval velocity represents the velocity of a single layer. Interval velocity is calculated from the stacking velocity using the Dix Equation (Equation 3). The interval velocity is the velocity used in migration to get an accurate geologic model since the velocity represents a single layer. If the velocity is too fast, the migrated results will show structures that look like smiles, if it is too slow the results will show frowns.

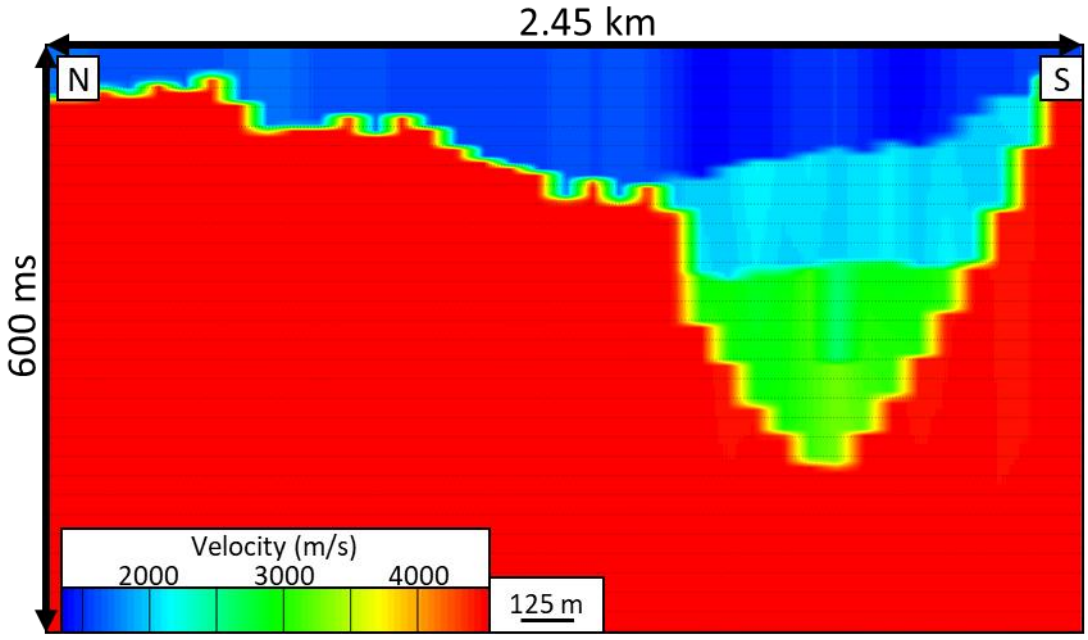

Figure 35: Final Velocity Model
The velocity model was manually corrected for the effects of the bowtie and to allow for proper migration of the data.

4.4 Migration

Migration is used to move reflectors that might be dipping or have complex structures into their correct location, horizontally and vertically, within the subsurface to create an accurate geologic image of the subsurface. The CMP stack assumes the reflector is directly below the CMP location, but when there are complex structures and steep dips, this is not true. Migration aims to reconstruct the true geologic image.

Post-stack migration migrates the data from the CMP stack. CMP stacks average the data from the different offsets since they are stacked together and limit the data from the far offsets. The far offsets are needed to image steeply dipping beds. Since post-stack migration is applied to the CMP stack, steeply dipping beds will still not be imaged correctly. CMP stack is created using stacking velocities which are independent of dip. When two events with different dips intersect each other, only one stacking velocity can be used, meaning one of the events will be stacked with the incorrect velocity. Pre-stack migration migrates the unstacked shot gathers and correctly images steeply dipping beds since it uses all the offset data. Another option is Dip-moveout correction (DMO). It is applied to gathers after NMO corrections but before the CMP stack. NMO corrects for moveout caused by linear events (Equation 2), and DMO corrects for the moveout caused by dipping events. (Equation 4). The dipping events are preserved, and the data are stacked and represent a result similar to pre-stack migration.

$$t^2 = t_0^2 + \frac{x^2 cos^2(\phi)}{v^{2v}};\ v_{NMO} = \frac{v}{\cos(\phi)}$$

Equation 4: Travel Time for Dipping Reflector
V_{NMO} = stacking velocity; v = velocity; ϕ = dip; t = travel time; t0 = travel time at 0 offset; x = offset

DMO was attempted in the study, but problems with the tools used in Promax prevented a result. The tool removed a portion of the data in the Northern line, and so the results were not trusted. Reasons for this error were not successfully determined, thus results are excluded from this thesis.

Post-stack Migration

Post-stack migration migrates the data after the CMP stack is finalized. Iterative Stolt method was used for the post-stack migration. Iterative Stolt method uses a single velocity gradient and operates in the F-K (frequency – wave number) domain (Promax Reference). Other migration methods including finite-difference implicit and explicit migrations were tested, but the Iterative Stolt gave the best results for post-stack (Figure 36a). The post-stack migration results are in the time domain and are converted to the depth domain using the interval velocity model. The final datum is applied to the line (Figure 36b). There is a clear U-shaped structure in the southern portion, but the sides of the structure are not imaged well since they have steep dips.

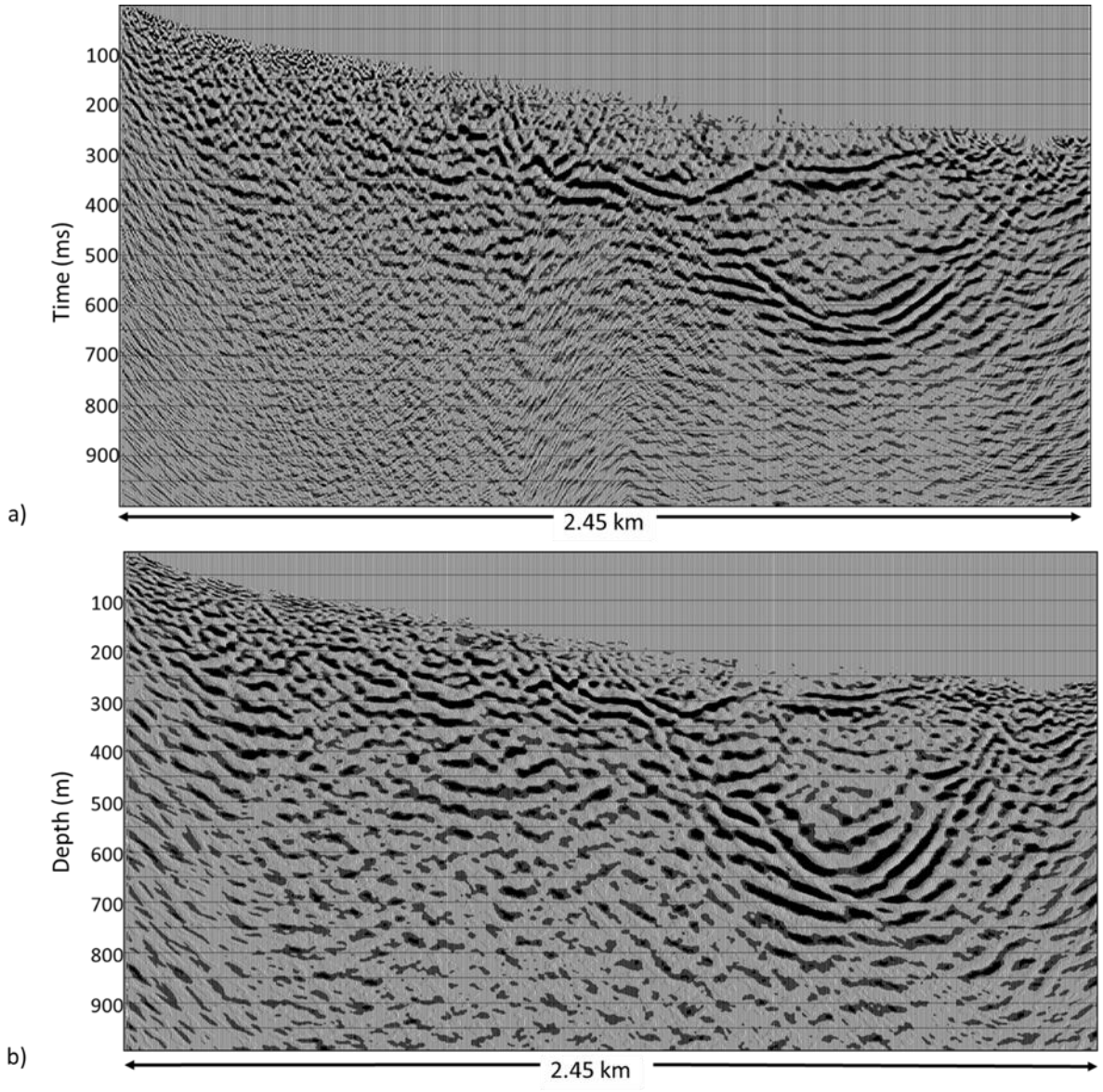

Figure 36: Post-stack Migration
Results from the post-stack migration displaying in time (a) and depth (b). Both images fail to image the steep sides of the u-shaped structure.

Pre-Stack Migration

Structures that have complex geometries with differing dips are better imaged through pre-stack migration. Pre-stack migration was used in this study to attempt to better image the sides of the u-shaped structure in the southern end of the survey. The Kirchhoff migration method was used for the pre-stack migration. Kirchhoff uses the interval velocities to calculate the travel times for the events and to determine the location of the reflectors. A migration aperture of 500 m was used. Aperture width is determined by the number of traces which show the reflector in the CMP stack. In this case, the basement reflectors that form the bowtie structure are around 500 m wide. After the migration, the individual events with differing dips will be in the right place, and the data are correctly stacked (Figure 37a). The pre-stack migration was depth converted using the interval velocity and moved to the final datum (Figure 37b). The pre-stack migration was able to better image the sides of the u-shaped structure in the southern portion of the survey and will be used for interpretation over the post-stack results.

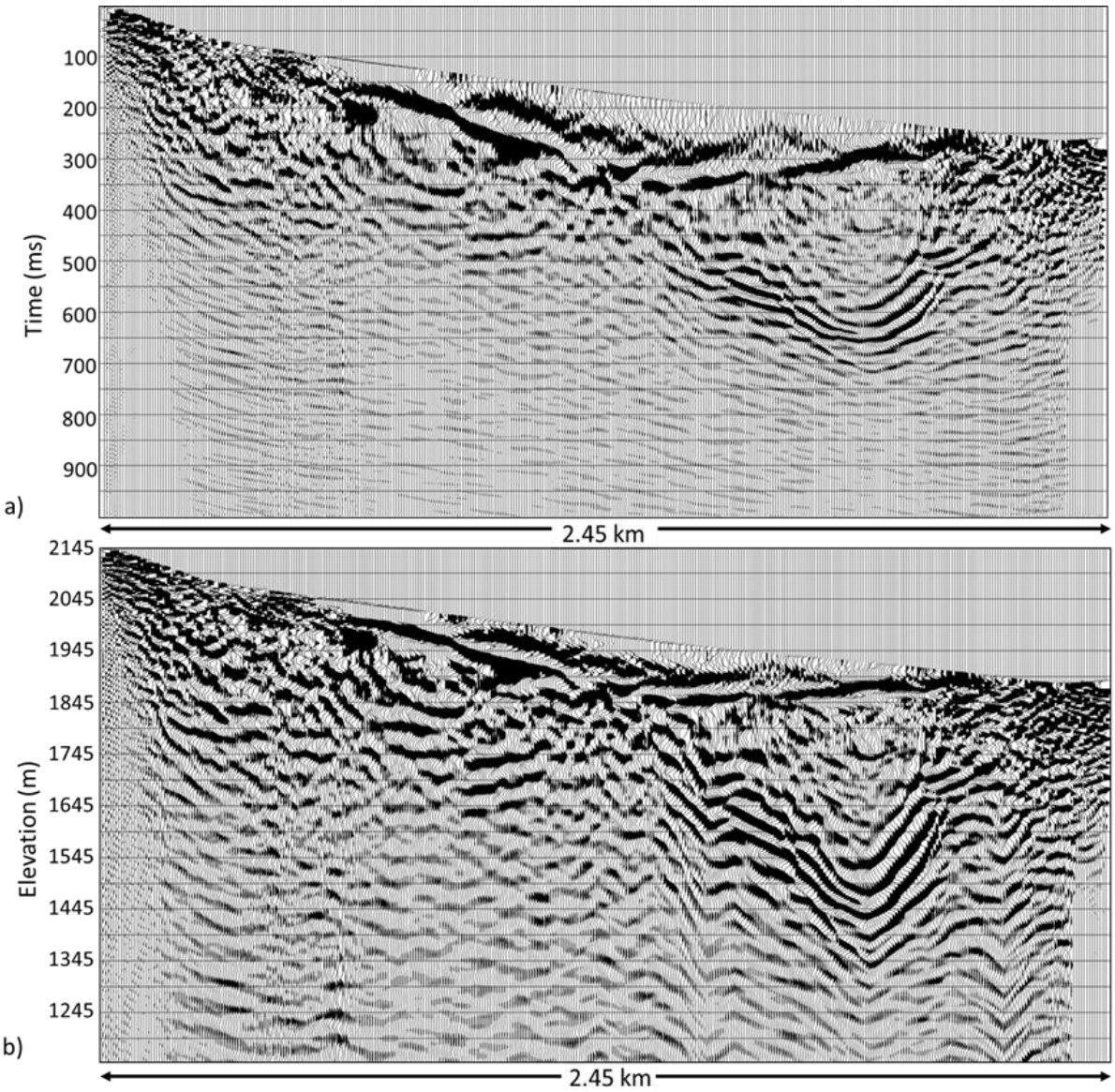

Figure 37: Pre-stack Migration
Results of the pre-stack migration in time (a) and depth (b). The depth conversion narrows the U-shaped structure and better images of the steep sides.

Chapter 5: Interpretation

5.1 Precambrian Basement

The pre-stack migration results are used for interpretation because they better image the steep dips apparent in the structure of the subsurface (Figure 37b). On the southern segment of the line, there are clear u-shaped horizons that match with the area lacking high velocities in the tomographic model. These horizons are interpreted to be the Precambrian basement. There are multiple U-shaped horizons present due to the complex structure of the basement in three dimensions. When a 2D seismic line is processed, it is assumed that the structure does not change perpendicular to the line. The seismic image is interpreted to represent the structure under the line only (Drummond et al., 2004). In cases of dips perpendicular to the line, out-of-plane structures can create multiple reflectors that appear stacked on top of each other (Drummond et al., 2004). The multiple reflections in the U-shaped structure in the southern part of the line are interpreted to represent out-of-plane reflections. Out-of-plane structures suggest that Precambrian basement is different elevations along the longitudinal direction of the canyon. Over-deepening caused by glacial processes occurs along the longitudinal axis since that is the direction of ice flow. Differing elevations along the basement instead of a smooth profile suggest over-deepening.

The Precambrian basement outcrops at 1662 m in the western mouth of the canyon and around 1890 m in the northeastern portion (Soreghan et al., 2015). The reflection seismic results suggest an elevation between 1400-1520 m for the lowest point of the basement (Figure 38). This proves over-deepening since the basement is lower than the outcrops at the mouths of the canyon, therefore below the fluvial grade. The multiple reflections constrain the total depth-to-basement in the over-deepened section to the range of 400-500 m.

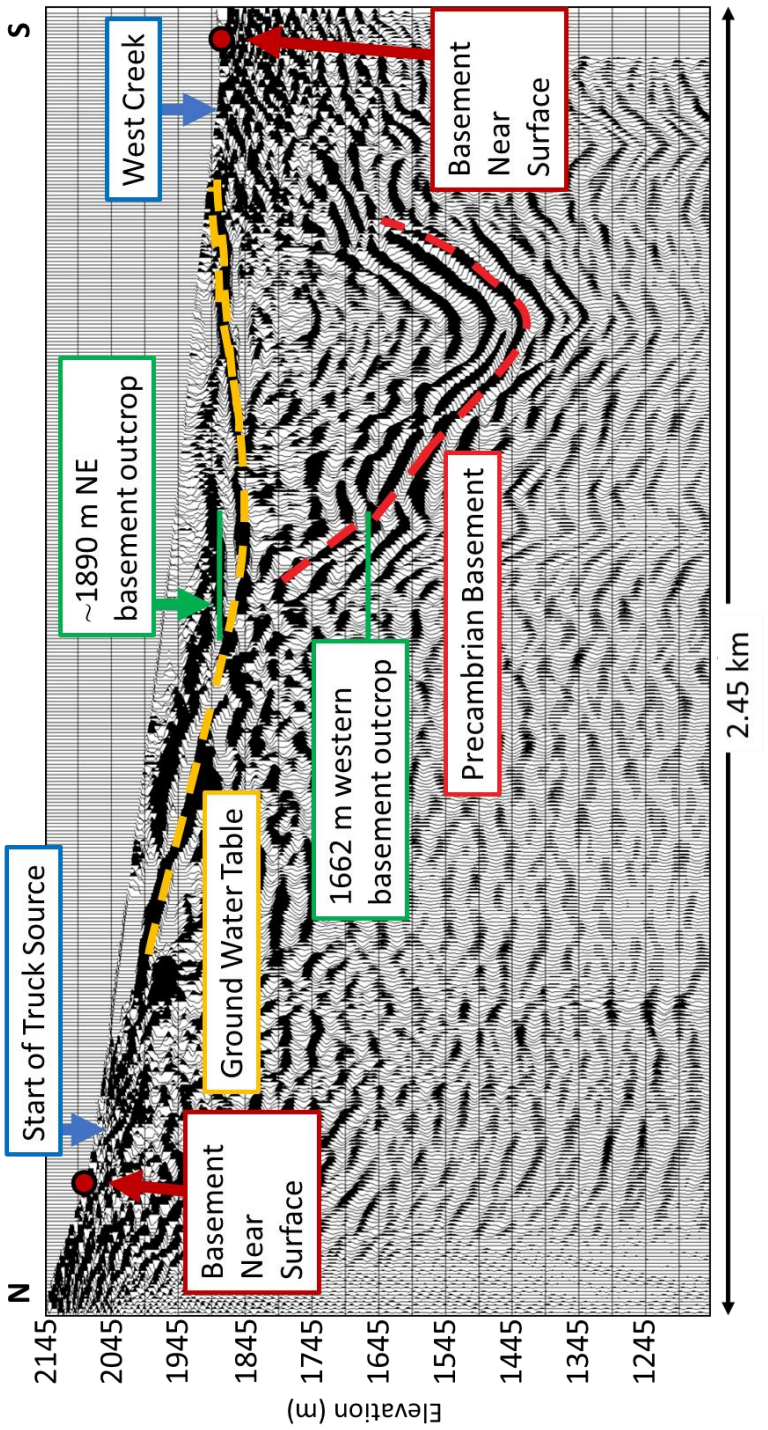

Figure 38: Pre-stack Migration Result Interpretation
Pre-stack migration results with interpretations of the groundwater table and Precambrian basement. The Precambrian basement is not distinguishable in the image on the very northern and southern portions of the line, but it has a clear u-shaped structure where visible.

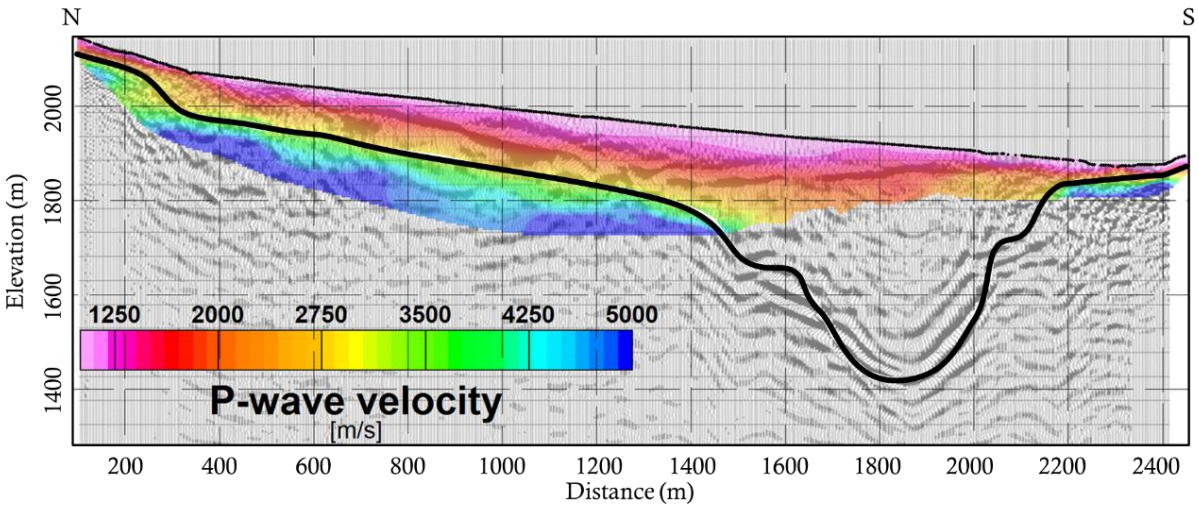

Figure 39: Precambrian Basement Interpretation
Modified from Behm at al., 2019. All results from the reflection processing, tomography model, and a delay time model (Behm et al., 2019) are used to create a final interpretation of the Precambrian basement structure (black line).

5.2 Upper Reflector

The upper reflector is visible in the profile between 600 - 1200 m and has an elevation between 1845 - 1945 m (Figure 38). Over-laying the reflection processing results with the tomographic model displays the upper reflector to be around velocity isoline 1500 m/s (Figure 39). The Precambrian basement reflector would be deeper around isoline 3000 m/s, which is supported by a delay time model created by Behm et al. (2019). 1500 m/s is the velocity of saturated sand (Whightman et al., 2003), suggesting that the first reflector indicates the water table. Further work is needed to test the suggestion that the upper reflector is the water table.

The Precambrian basement is not imaged in the northern part of the survey (Figure 38). The basement is hypothesized to be within a few meters of the surface in this area and weathered since it is close to the surface. Weathering lowers the velocity, causing a gradual increase in velocity instead of a sharp impedance contrast, reducing the chance of imaging over background noise. The sledgehammer was also used as a source in the northern portion, producing lower

energy than the truck-mounted source, which might have hampered imaging. The north portion also had more traces killed due to the overlap between the sledgehammer and truck-mounted shots. Trace killing lowers the fold of the data. The area already had low fold, and further reductions in the fold could decrease the signal to noise ratio.

A clear Precambrian basement reflector is not visible in the last 200 m of the line in the south (Figure 38). Likely the noise in this area from the creek and the nearby highway masked the signal. Shots were also skipped in this area since the acquisition truck could not drive near the creek. The basement is also closer to the surface and increases in weathering could have prevented imaging. The tomographic model is used to interpret the basement in the northern and southern portion of the line (Figure 39).

5.3 Velocities

Average velocity values of metamorphic rock range from 2,400 to 6,000 m/s depending on the amount of weathering (Whightman et al., 2003). The Precambrian basement is composed of metamorphic rock in Unaweep Canyon, and from the tomographic model, the velocity ranges from 3000 – 4500 m/s, which is within the range of metamorphic rock. The faster tomographic velocities are absent in the southern portion fitting with the stacking velocities that appear deeper. The velocity model (Figure 31, 35) also suggests that the Precambrian basement has steep sides that emphasizes the U-shaped seen in the pre-stack migration model.

Figure 40 compares the velocities from a sonic log from the well Massey #2 to the interval velocities calculated from the picked stacking velocities. The well is located 5 km from the line and is also at a higher elevation, so there are likely some differences within the subsurface between the two localities including water saturation and clast size within the upper fanglomerate. The sonic log shows two distinct velocity layers, the fanglomerate that covers the

canyon floor around 2000 to 2500 m/s and the layer identified in the core as a lacustrine layer around 1700 m/s (Soreghan et al., 2007). The interval and stacking velocities show four distinct velocity layers, the first layer around 1500 m/s, second layer around 1900 m/s, the third layer at around 2700 m/s, and the fourth layer around 4500 m/s; the latter interpreted to be the metamorphic Precambrian basement.

The velocity model layers should have higher velocities than layers at the well site since higher dips increase the stacking velocity (Equation 4). The second velocity layer of the sonic log and the interval velocities are similar, leading to the conclusion that the second layer seen in the data correlates to the lacustrine sediment found in the core. The first layers of the well and data vary significantly. A possible reason is differences in water saturation between the well and the survey localities. They are 5 km apart, the well is at a higher elevation, and coring occurred 14 years before the seismic acquisition (and in different seasons of the year). Water saturation in shallow sediment layers and soils increases the P-wave velocity (Prasad et al., 2004). The increase in P-wave velocity suggests that the well location might consist of a saturated fanglomerate while at the survey location it is dry in the same elevation interval. This fact is further supported by a lower Vp/Vs ratio within the fanglomerate and a higher Vp/Vs ratio in the lacustrine sediment indicating a dry upper layer and a saturated second layer (Behm et al., 2019). The well had a third layer of sediments consisting of mostly clay mud within the core, but since it was only the last couple meters, the sonic log was not taken over the layer (Soreghan et al., 2007). However, this transition matches with the presence of the third layer that was seen in the velocity log.

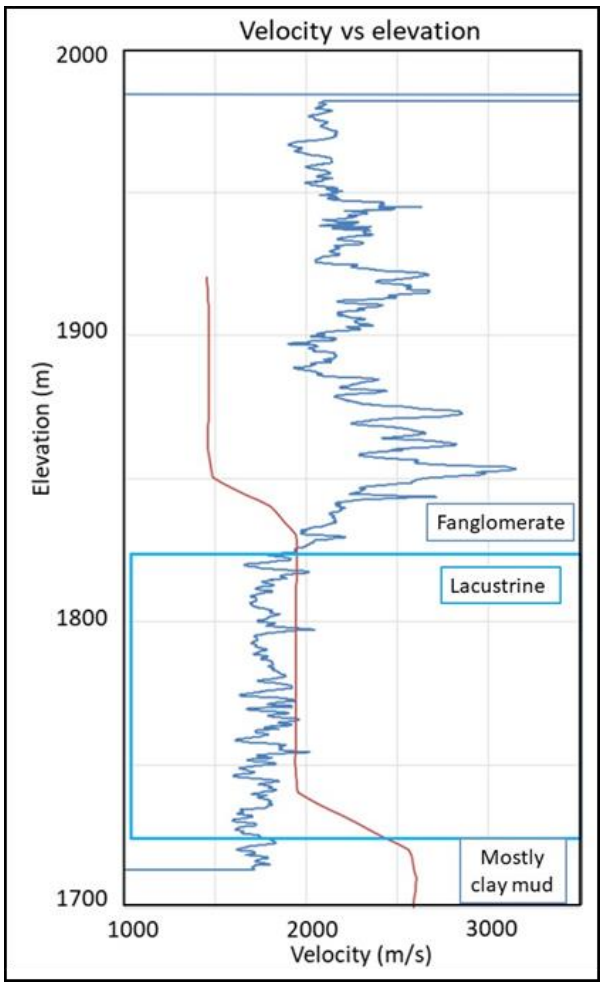

Figure 40: Seismic Velocities vs. Well Sonic Log
The interval velocities (red) are compared to the sonic log values (blue) from Massey #2. The well was at a higher elevation and 5 km away from the survey and is placed accordingly in the figure. The figure is modified from Behm et al. (2019).

5.4 Geologic Implications

The results from this study indicate that the Precambrian basement is at a depth that is over-deepened relative to the (ancient) fluvial base level and that the cross-sectional geometry of the valley here is U-shaped. No major faults were detected in the survey, nor expressed on the surface in the survey area that could have caused such features. The U-shaped, over-deepened profile is most readily explained as the result of alpine glaciation in the past, like other alpine

glaciers imaged through geophysical methods (de Franco et al., 2009; Brueckl et al., 2010; Bleibinhaus and Hilberg, 2012; Pomper et al., 2017.).

Although only glaciation can create over-deepening, the age of the glaciation remains in question. A Quaternary age is unlikely given the current elevation of Unaweep Divide (see Introduction), suggesting an earlier glaciation, during an older "icehouse" time in Earth history. Earlier icehouses times include the late Paleozoic glaciation (Soreghan et al. 2007, 2008, 2014, 2015) or an even older glaciation. An older glaciation seems unlikely since this would require landforms preservation over many hundreds of millions of years (Twidale, 2003) and there is evidence including the hypothesized age of the last layer in the well supporting a late Paleozoic age. Further evidence of a late Paleozoic age is given by the onlap of an (controversially) interpreted proglacial deposit on the Precambrian basement on the western mouth of Unaweep Canyon (Soreghan et al., 2009). However, the hypothesis of Paleozoic glaciation is also challenged (Aslan et al., 2008, 2014; Hood et al., 2009). To support glaciation during the late Paleozoic, the canyon would need to be at a higher elevation than previously modeled or the climate was colder than current climate models suggest.

Several areas for future research remain. A key question is how to preserve a landscape from the late Paleozoic in an active orogenic zone. Also, confirmation of the minimum age of the basement surface requires dating the layer lying directly atop the basement, which requires coring this interval. Glacial origin of Unaweep Canyon suggests the possibility of additional paleo-glacial valleys undetected in the subsurface near the canyon. Answering this would help assess the extent of possible ancient mountain glaciation.

In conclusion, the reflection seismic line traversing western Unaweep Canyon shows a clear over-deepened and U-shaped structure that is interpreted to be the result of past alpine

glaciation. Comparing the Precambrian basement depth along the seismic line with up- and downstream basement outcrops, it is established that Unaweep Canyon is over-deepened. Given the absence of evidence for Quaternary glaciation, the late Paleozoic glaciation hypothesis (Soreghan et al. 2007, 2008, 2014, 2015) is considered as the most likely cause for the observed over-deepening.

References

Aslan A, Karlstrom K, Hood W, Cole RD, Oesleby T, Betton C, Sandoval M, Darling A, Kelley S, Hudson A, Kaproth B., 2008, River incision histories of the Black Canyon of the Gunnison and Unaweep Canyon: Interplay between late Cenozoic tectonism, climate change, and drainage integration in the western Rocky Mountains, in Raynolds, R.G., ed., Roaming the Rocky Mountains and environs: Geological fi eld trips: Geological Society of America Field Guide 10, p. 175–202, doi: 10 .1130 /2008 .fl d010 (09) .

Aslan, A., Hood, W.C., Karlstrom, K.E., Kirby, E., Granger, D.E., Kelly, S., Crow, R., Donahue, M.S., Polyak, V., and Asmerson, Y., 2014, Abandonment of Unaweep Canyon (1.4–0.8 Ma), western Colorado: Effects of stream capture and anomalously rapid Pleistocene river incision: Geosphere, v. 10, doi: 10 .1130 /GES00986 .1 .

Balco, G., Soreghan, G.S., Sweet, D.E., Marra, K.M., and Bierman, P., 2013, Cosmogenic-nuclide burial ages for Pleistocene sedimentary fi ll in Unaweep Canyon, Colorado, USA: Quaternary Geochronology, v. 18, p. 149–157, doi: 10 .1016 /j .quageo .2013 .02 .002 .

Behm, M., Brückl, E., Chwatal, W., and Thybo, H., 2007, Application of stacking and inversion techniques to three-dimensional wide-angle reflection and refraction seismic data of the Eastern Apls: Geophysical Journal International, v. 170, p. 275-298, doi: 10.1111/j.1365-246X.2007.03393.x.

Behm, M., Cheng, F., Patterson, A., and Soreghan, G., 2019, Passive processing of active nodal seismic data: Estimation of Vp/Vs – rations to characterize structure and hydrology of an alpine valley infill: Solid Earth, in review.

Bleibinhaus, F., and Hilberg, S., 2012, Shape and structure of the Salzach Valley, Austria, from seismic traveltime tomography and full waveform inversion: Geophys. J. Int., v. 189, p. 1701–1716, doi: 10.1111/j.1365-246X.2012.05447.x.

Brückl, E., Brückl, J., Chwatal, W., and Ullrich, C., 2010, Deep alpine valleys: Examples of geophysical explorations in Austria: Swiss Journal of Geoscience, v. 103, p. 329–344, doi: 10.1007/s00015-010-0045-x.

Carter, F.W., 1966, Age of the Uncompahahgre Uplift and Unaweep Canyon, west-central Colordado: U.S. Geological Survey Professional Paper 550-C, p. C86-C92.

Cole, R.D., and Young, R.G., 1983, Evidence for glaciation in Unaweep Canyon, Mesa County, Colorado, in Averett, W.R., ed., Northern Paradox Basin-Uncompahgre Uplift (Grand Junction Geological Society Field Trip Guidebook): Grand Junction, Colorado, Grand Junction Geological Society, p. 73-80.

Condon, S.M., 1997, Geology of the Pennsylvanian and Permian Cutler Group and Permian Kaibab Limestone in the Paradox Basin, southeastern Utah and southwestern Colorado: U.S. Geological Survey Bulletin 2000-P, 46 p.

Davogustto, O.E., 2006, Soneo Gravimetrico en el Canon Unaweep: En Busca del Basamento y su Forma, B.S. Thesis, Simon Bolivar University, Caracas, Venezuela.

Drummond, B.J., Hobbs, R.W., and Goleby, B.R., 2004, The effects of out-of-plane seismic energy on reflections in crustal-scale 2D seismic sections: Tectonophysics, v. 388, p. 213–224, doi:10.1016/j.tecto.2004.07.040.

Everett, M, 2013, Near surface applied geophysics: Cambridge University Press.

de Franco, R., Biella, G., Caielli, G., Berra, F., Guglielmin, M., Lozej, A., Piccin, A., and Sciunnach, D., 2009, Overview of high resolution seismic prospecting in pre-Alpine and Alpine basins: Quaternary International, v. 204, p. 65–75, doi: 10.1016/j.quaint.2009.02.011.

Gannett, H., 1882, The Unaweep Cañon (Colorado): Popular Science Monthly, v. 20, p. 781–786.

Graphics, Landmark, 1995, ProMAX reference manual: Advance Geophysical Corp..

Hole, J.A., 1992, Nonlinear high-resolution three-dimensional seismic travel time tomography: Journal of Geophyscal Research, v. 97, p. 6553-6562.

Hood, W., Cole, R., and Aslan, A., 2009, Anomalous cold in the Pangaean tropics: Comment: Geology, v. 37, p. e192, doi: 10 .1130 /G30035C .1.

Lawton, D.C., Gallant, E.V., Bertram, M.B., Hall, K.W., and Bertram, K.L., 2013, A new S-wave seismic source: CREWES Research Report, v. 25.

Linton D.L., 1963, The forms of glacial erosion: Transactions and Papers Institite of British Geographers, v. 33, p. 1-28.

Lohman, S.W., 1981, Ancient drainage changes in and south of Unaweep Canyon, southwestern Colorado, in Epis, R.C., and Callender, J.F., eds., Western Slope Colorado: New Mexico Geological Society 32nd Field Conference Guidebook, p. 137–143.

Haffener, J., 2015, Gravity modeling of Unaweep Canyon: Determining Fluvial or Glacial Origins: B.S. Thesis, University of Oklahoma, Norman, Oklahoma.

Hart, B.S., 2010, Introduction to seismic interpretation: AAPG Discovery Series No. 16, AAPG Datapages.

Marra, K.M., 2008, Late Cenozoic geomorphic and climatic evolution of the northeastern Colorado Plateau as recorded by Plio-Pleistocene sediment fi ll in Unaweep Canyon, Colorado [M.S. thesis]: Norman, University of Oklahoma, 160 p.

Maxwell, P., and Lansley, M., 2011, What receivers will we use for low frequencies?: SEG Technical Program Expanded Abstracts,. P. 72-76.

McQuarrie, N., and Chase, C.G., 2000, Raising the Colorado Plateau: Geology, v. 117, no. 1, p. 91-94.

Oesleby, T.W., 1978, Uplift and deformation of the Uncompahgre Plateau: Evidence from fi ll thickness in Unaweep Canyon, west-central Colorado [M.S. thesis]: Boulder, University of Colorado, 122 p.

Porter, S.C., 2000, Snowline depression in the tropics during the last glaciation: Quaternary Science Reviews, v. 20, p. 1067–1091, doi: 10.1016/S0277-3791(00)00178-5.

Prasad, M., Zimmer, M.A., Berge, P.A., and Bonner, B.P., 2004, Laboratory measurements of velocity and attenuation in sediments: UCRL-JRNL- 205155.

Peale, A.C., 1877, Geological report on the Grand River district: U.S. Geological and Geophysical Survey of the Territories, Ninth Annual Report, p. 31-102

Pomper, J., Salcher, B.C., Eichkitz, C., Prasicek, G., Lang, A., Lindner, M., and Götz, J., 2017, The glacially overdeepened trough of the Salzach Valley, Austria: Bedrock geometry and sedimentary fill of a major Alpine subglacial basin: Geomorphology, v. 295, p. 147–158, doi: 10.1016/j/geomorph.2017.07.009.

Price, R., Karlstrom, K.E., Donahue, M., Aslan, A., and Pecha, M., 2012, Detrital zircon analysis of high terraces of the early Colorado River system (Crooked Ridge River, Grand Mesa, and upper Green River): Implications for Colorado Plateau drainage evolution: Geological Society of America Abstracts with Programs, v. 44, no. 6, p. 20.

Rojas Y., 2007, Acquisition, Processing and Modeling of Shallow Seismic Reflraction and Reflection profiles: Unaweep Canyon, Colorado: M.S. thesis, University of Oklahoma,

Scott, R.B., Harding, A.E., Hood, W.C., Cole, R.D., Livaccai , R.F., Johnson, J.B., Shroba, R.R., and Dickerson, R.P., 2001, Geologic map of Colorado National Monument and adjacent areas, Mesa County, Colorado: U.S. Geological Survey Geologic Investigations Series I-2740.

Sheriff, R., and Geldart, L.P., 1995, Exploration seismology: Cambridge Press, ed. 2.

Soreghan, G., Sweet, D., Marra, K., Eble, C., Soreghan, M., Elmore, R., Kaplan, S., and Blum, M., 2007, An exhumed late Paleozoic canyon in the Rocky Mountains: Journal of Geology, v. 115, p. 473–481, doi: 10.1086 /518075 .

Soreghan, G.S., Soreghan, M.J., Poulsen, C.J., Young, R.A., Eble, C.F., Sweet, D.E., and Davogustto, O.C., 2008, Anomalous cold in the Pangaean tropics: Geology, v. 36, no. 8, p. 659–662, doi: 10.1130/G24822A.

Soreghan, G.S., Soreghan, M.J., Sweet, D.E., and Moore, K.D., 2009, Hot fan or cold outwash? Hypothesized proglacial deposition in the upper Paleozoic Cutler Formation, western tropical Pangea: Journal of Sedimentary Research, v. 79, p. 495-522, doi: 10.2110/jsr.2009.055.

Soreghan, G.S., Sweet, D.E., and Heavens, N.G., 2014, Upland glaciation in tropical Pangaea: Geologic evidence and implications for late Paleozoic climate modeling: Journal of Geology, v. 122, p. 137–163, doi: 10.1086 /675255 .

Soreghan, G.S., Sweet, D.E., Thomson, S.N., Kaplan, S.A., Marra, K.R., Balco, G., and Eccles, T.M., 2015, Geology of Unaweep Canyon and its role in the drainage evolution of the northern Colorado Plateau: Geosphere, v. 11, p. 320–341, doi:10.1130/GES01112.1.

Telford, W.M., Geldart, L.P., and Sheriff, R.E., 1990, Applied Geophysics: Cambridge University Press, v.1.

Twidale, C., 2003, The enigma of survival; problems posed by very old paleosurfaces: Physical Geography, v. 24, p. 26–60, doi: 10 .2747 /0272 -3646 .24 .1 .26 .

Wightman, W.E., Jalinoos, F., Sirles, P., and Hanna, K., 2003, Application of Geophysical Methods to Highway Related Problems: Federal Highway Administration, Central Federal Lands Highway Division, Lakewood, CO. Publication No. FHWA-IF-04-021.

Yeend, W.E., 1969, Quaternary geology of the Grand and Battlement Mesa area, Colorado: U.S. Geological Survey Professional Paper 617.

Yilmaz Ö., 2001, Seismic data analysis: Processing, inversion, and interpretation of seismic data: Society of exploration geophysicists.

Appendix A: Processing Flows and Parameters

Processing Flow

1. Geometry
2. Refraction Model Travel Times
3. Refraction Statics
4. Signal Processing and Muting
5. Velocity Analysis
6. NMO and Stack
7. Velocity Manipulation
8. Time Migration
9. Pre-Stack Migration

Pictures of the processing flow follow. The flows are presented exactly as run for the final model with the processes run highlighted in bold. Some flows have processes not highlighted in dark blue, these processes were tested to see if they improved the results or used to create background data needed for the flow. The majority of the processes used the pre-programed parameters but pictures of the parameters changed are also pictured.

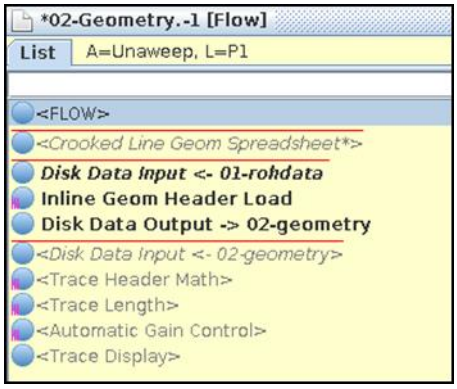

Figure 41: Geometry Flow

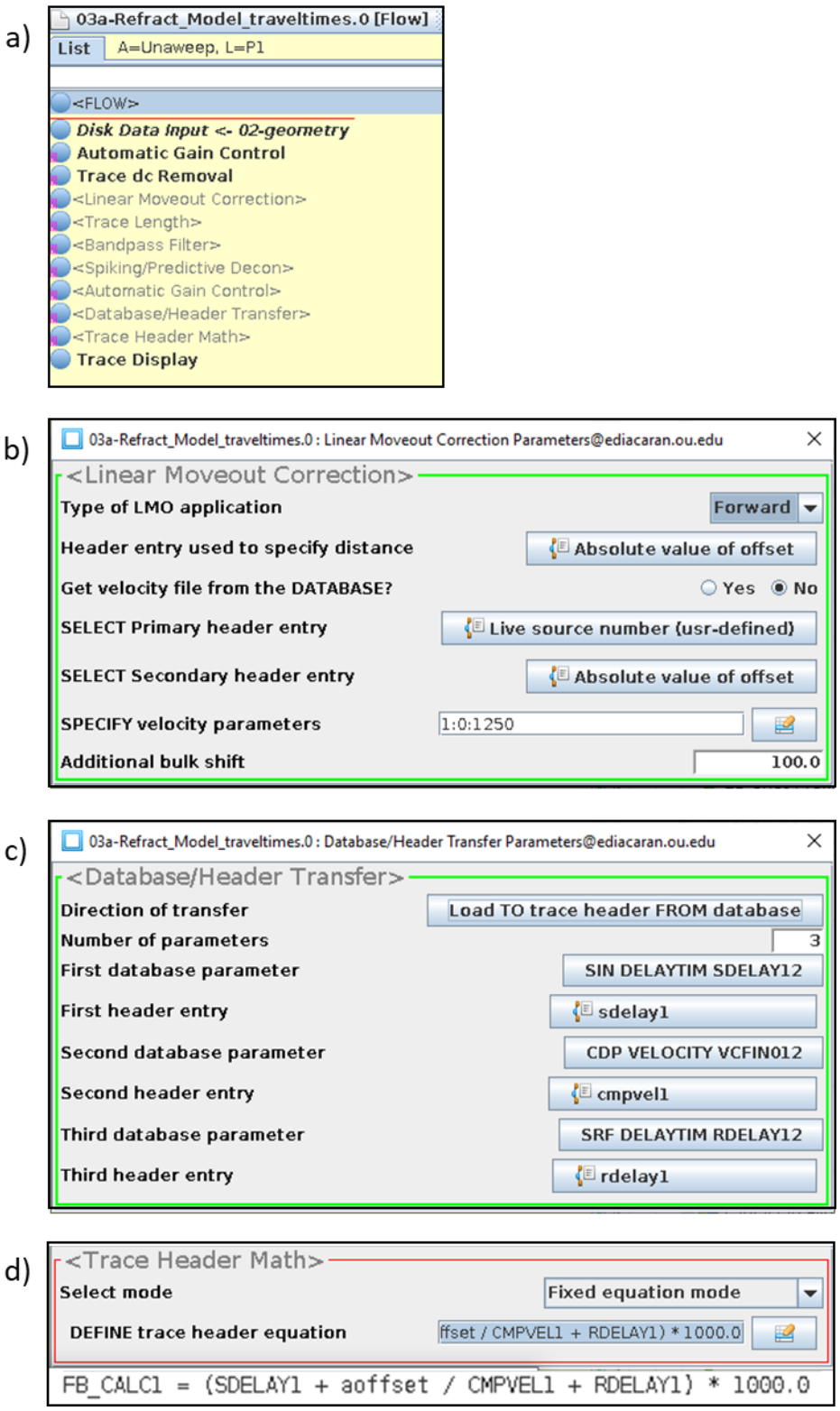

Figure 42: Refraction Model Travel Time Flow

a)

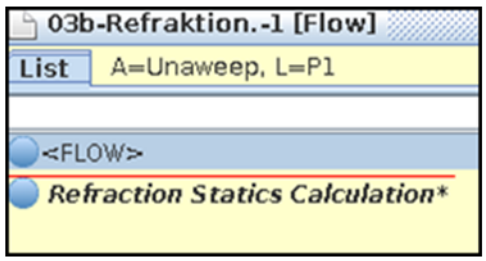

b)

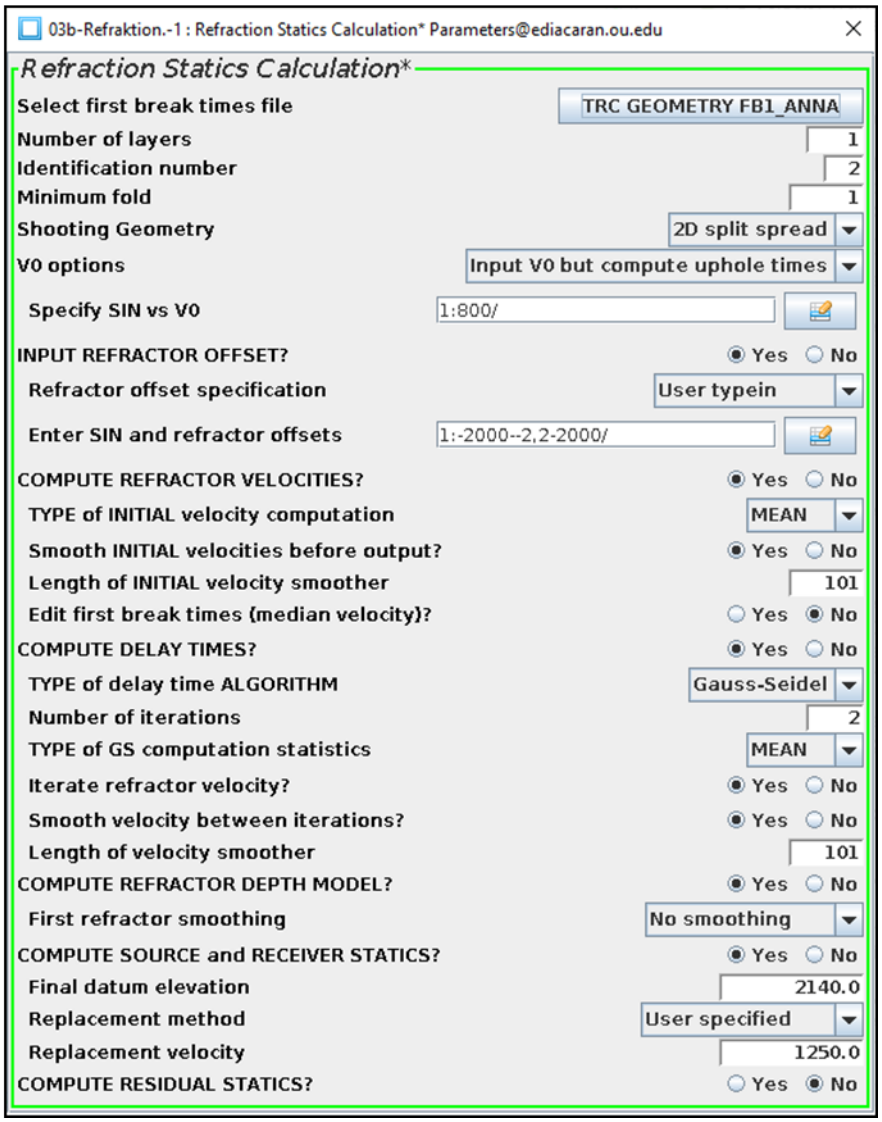

Figure 43: Refraction Statics Flow

a)

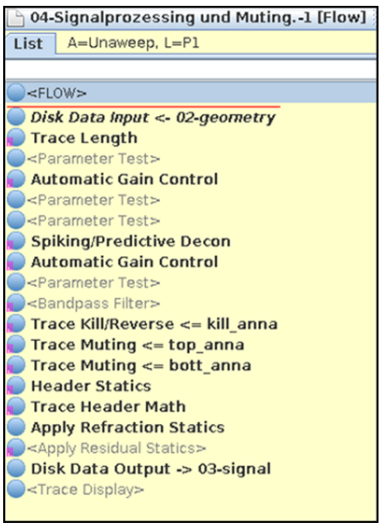

b)

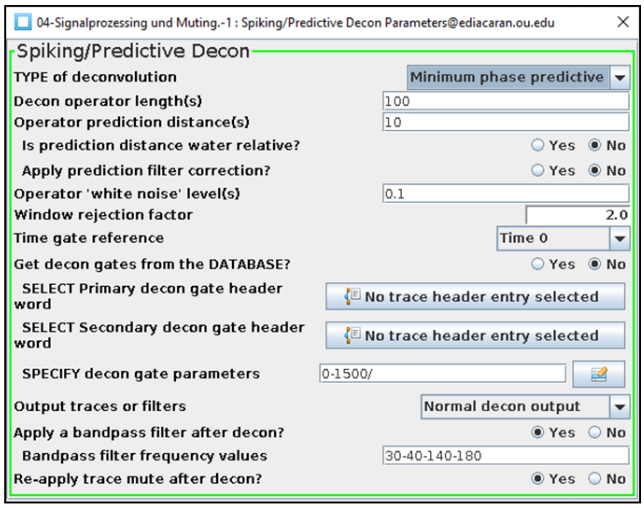

c)

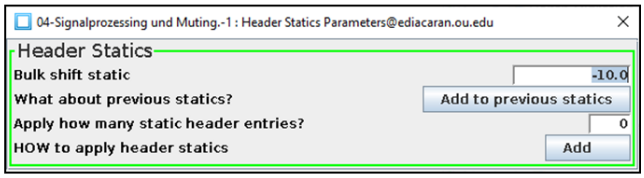

d)

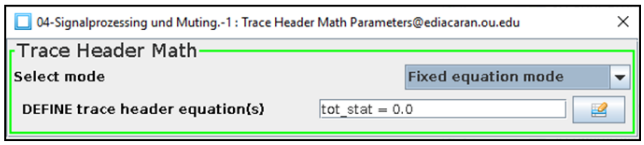

e)

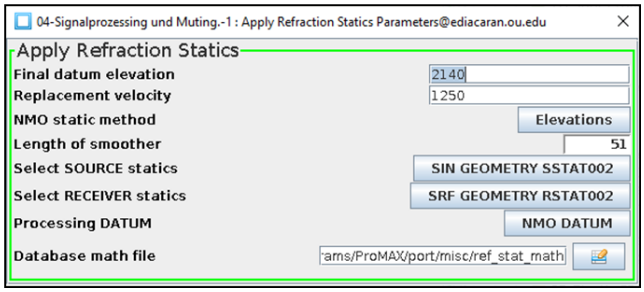

Figure 44: Signal Processing Flow

a)

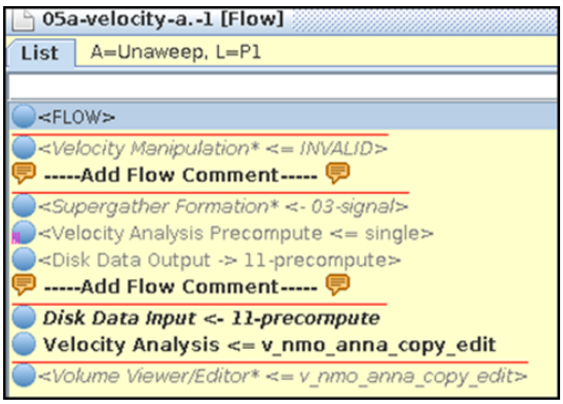

b)

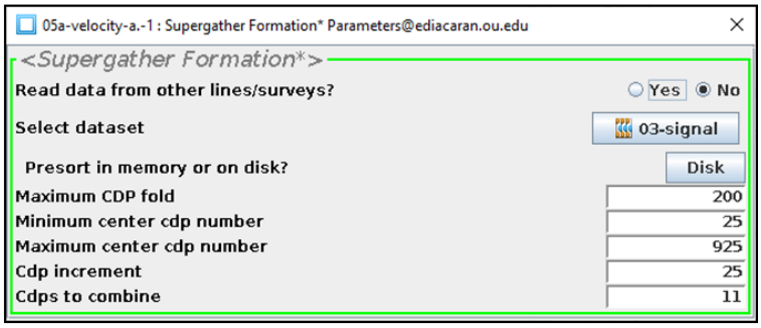

c)

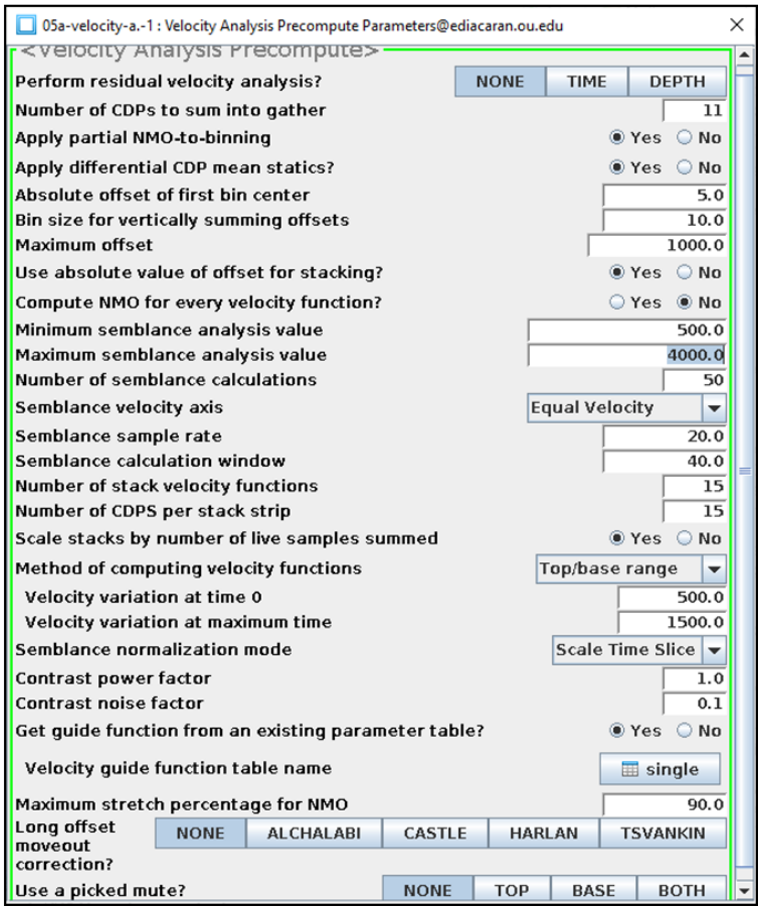

Figure 45: Velocity Analysis Flow

a)

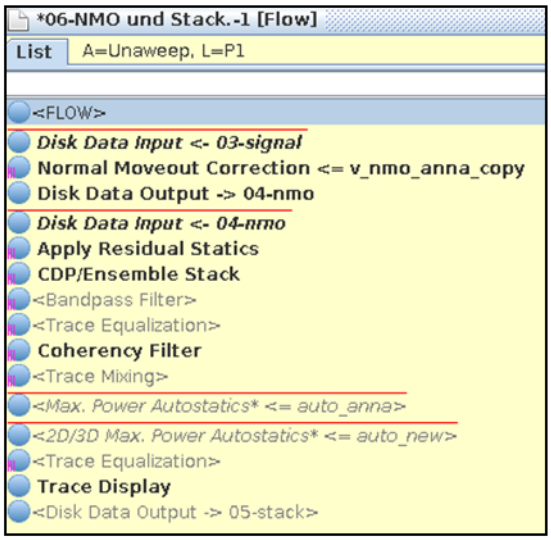

b)

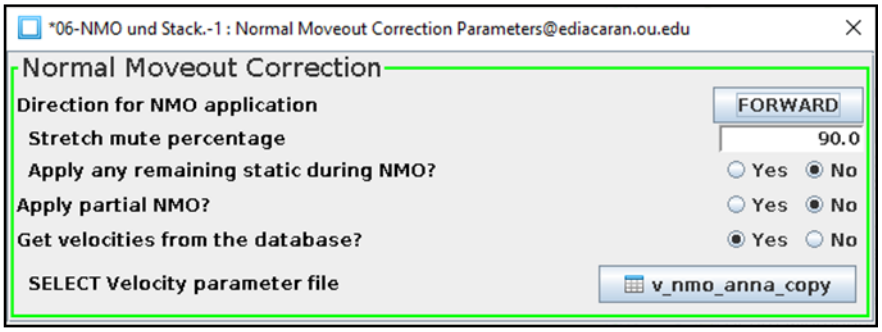

c)

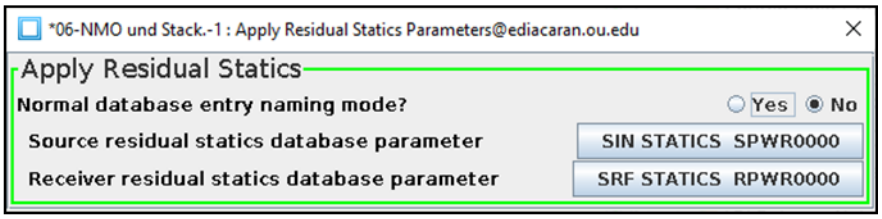

d)

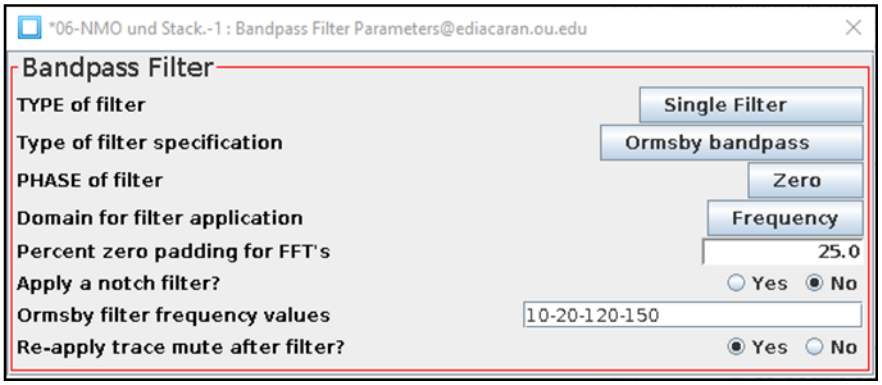

Figure 46: CMP Stack Flow

e)

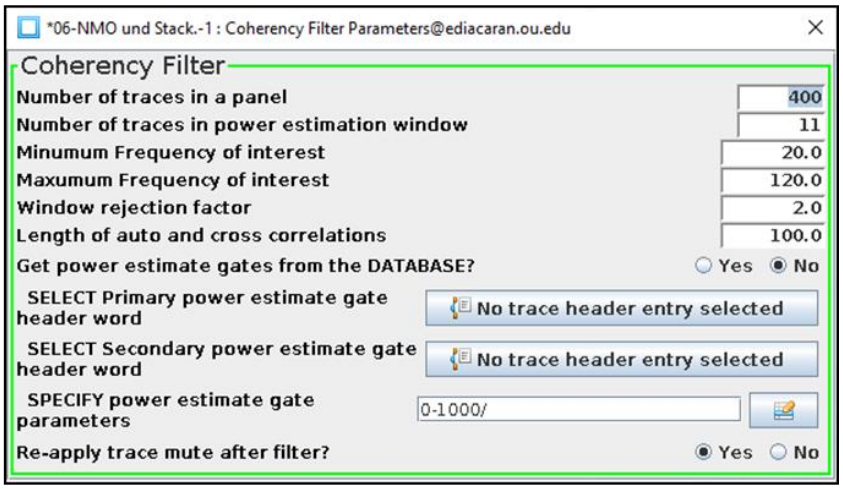

f)

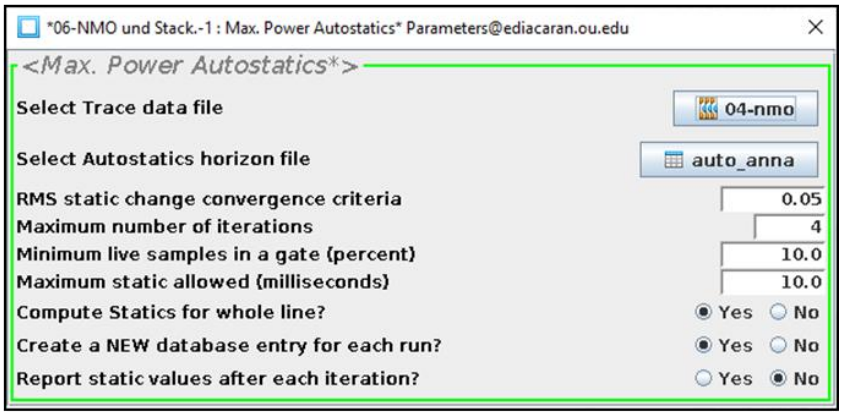

g)

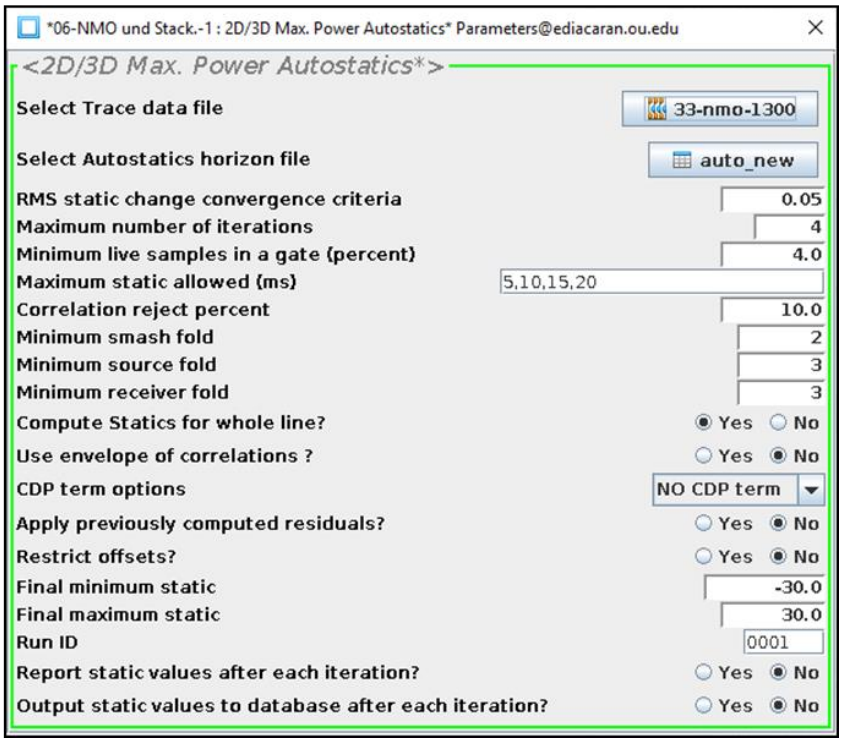

CMP Stack Flow Cont.

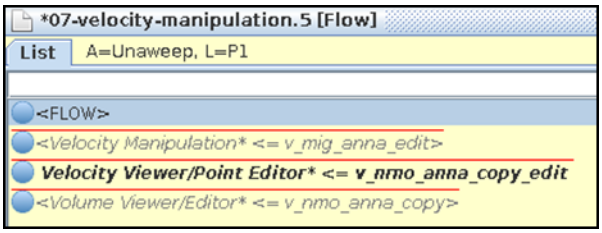

Figure 47: Velocity Manipulation Flow

a)

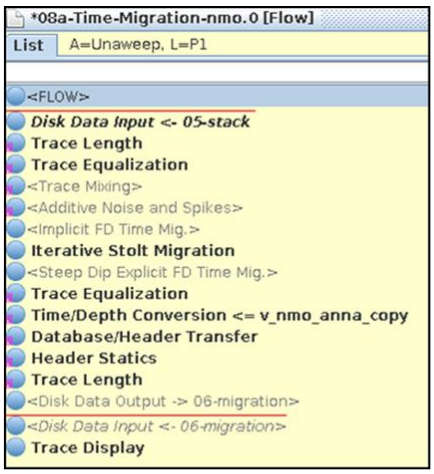

b)

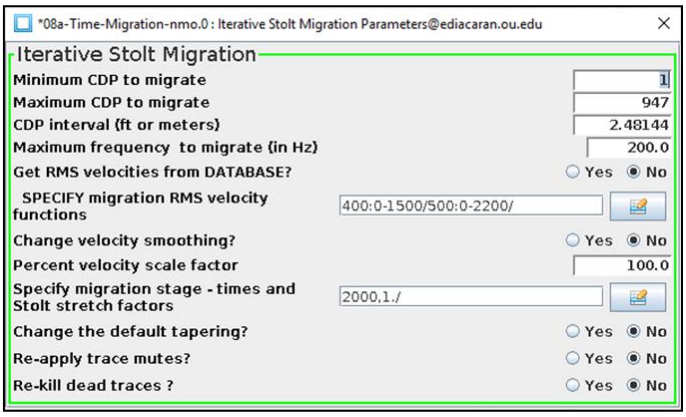

c)

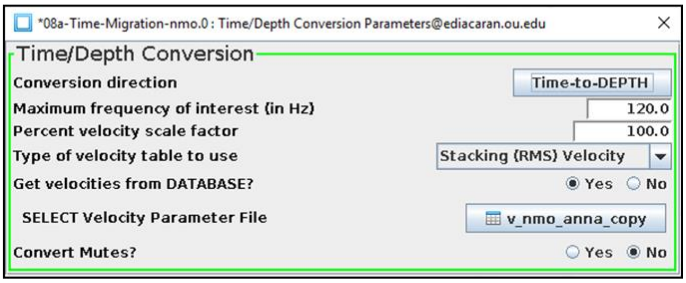

d)

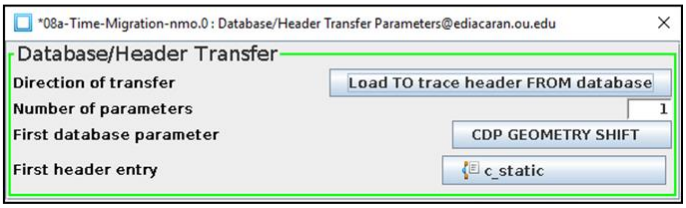

e)

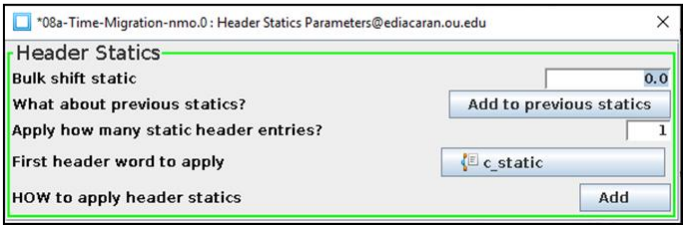

Figure 48: Post-stack Migration Flow

a)

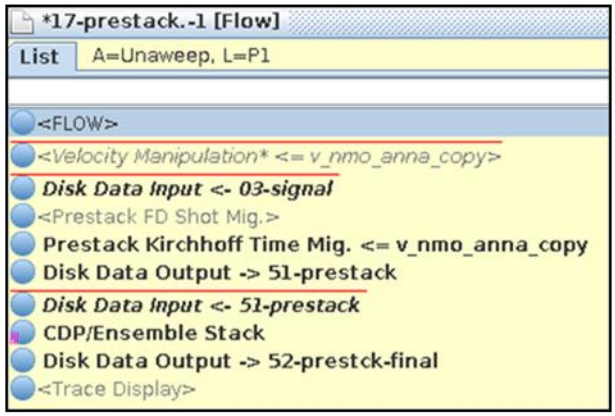

b)

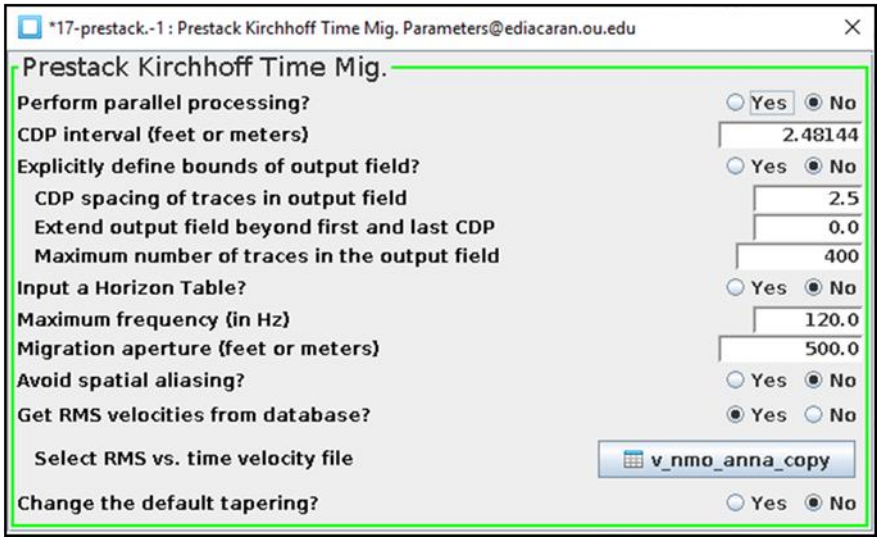

Figure 49: Pre-stack Migration Flow

Dataset	Process
01-rawdata	The raw data with no geometry applied.
02-geometry	The raw data with geometry applied.
03-signal	The geometry with signal processing applied.
04-nmo	The signal processing with NMO corrections.
05-stack	The CMP stack
06-migration_iterative-stolt	Post-stack migration results using iterative-Stolt method.
51-prestack	The unstacked results from pre-stack migration using Kirchhoff method.
52-prestack-final_Kirchhoff	The stacked after pre-stack migration.

Figure 50: Final Processing Dataset Names

Velocity Name	Type	Description
V_nmo_anna	VEL	Original velocity picked from the velocity analysis
V_nmo_anna_copy	VEL	Final stacking velocity model edited to reflect geology. Used to calculate interval velocity.
V_mig_anna_edit	VIT	Interval velocities calculated from the final stacking velocity model.

Figure 51: Final Velocity Models Used in Processing